Analysis of *Gaia* radial-velocity standards: stability and new substellar companion candidates

A. Boulkaboul,[1,2]★ Y. Damerdji,[1,3]★ T. Morel,[3]★ Y. Frémat,[4] C. Soubiran,[5] E. Gosset[3] and T. E. Abdelatif[1]

[1]*CRAAG – Centre de Recherche en Astronomie, Astrophysique et Géophysique, Route de l'Observatoire, Bp 63 Bouzareah, DZ-16340 Algiers, Algeria*
[2]*University of Science and Technology Houari Boumediene, Alia, DZ-16000 Algiers, Algeria*
[3]*Space sciences, Technologies and Astrophysics Research (STAR) Institute, Université de Liège, Quartier Agora, Allée du 6 Août 19c, Bât. B5c, B-4000 Liège, Belgium*
[4]*Royal Observatory of Belgium, av. circulaire 3, B-1180 Brussels, Belgium*
[5]*Laboratoire d'astrophysique de Bordeaux, Univ. Bordeaux, CNRS, B18N, allée Geoffroy Saint-Hilaire, F-33615 Pessac, France*

ABSTRACT

Our main aim is to test the non-variability of the radial velocity (RV) of a sample of 2351 standard stars used for wavelength calibration of the Radial Velocity Spectrometer (RVS) instrument onboard *Gaia*. In this paper, we present the spectroscopic analysis of these stars with the determination of their physical parameters by matching observed and synthetic spectra. We estimate the offset between different instruments after determining the shift between measured and archived RVs since the instrument pipelines use various numerical masks. Through the confirmation of the stability of the target RVs, we find 68 stars with a long-term variation having an acceleration that exceeds $10\,\mathrm{m\,s^{-1}\,yr^{-1}}$. This suggests a barycentric reflex motion caused by a companion. As activity phenomena may be the source of periodic and trend-like RV variations in stars with putative planetary companions, we analysed various activity indicators in order to check their correlations to the RV changes. Among the trend stars, 18 have a trend model scatter greater than $100\,\mathrm{m\,s^{-1}}$ over a time span from 10 to 12 yr. We also confirm that six stars with known substellar companions have a total model scatter, 3σ, exceeding the threshold set by *Gaia*, that is, $300\,\mathrm{m\,s^{-1}}$. In addition, TYC8963-01543-1, an SB2 star, has data scatter $\sigma = 176.6\,\mathrm{m\,s^{-1}}$. Four more other stars are revealed to be variable after combining data from different instruments. Despite the presence of low-amplitude changes, a very large fraction of our sample (98.8 per cent) appears suitable as RV calibrators for *Gaia* RVS.

Key words: techniques: radial velocities – stars: activity – (stars:) binaries: spectroscopic – stars: fundamental parameters.

1 INTRODUCTION

According to Raghavan et al. (2010), the fraction of main-sequence, solar-type stars with stellar or brown dwarf companions is 46 ± 2 per cent. The orbital periods are generally long (distribution peaks at $\log P\,[\mathrm{d}] = 5.03$). Since stellar multiplicity plays a major role in the formation and evolution of stars, several surveys have investigated the occurrence of multiplicity. As an illustration, single-lined (SB1) and double-lined (SB2) spectroscopic binaries make up 33 per cent of the multiple systems in the catalogue of Raghavan et al. (2010), while the SB1 proportion in the *Gaia*-European Southern Observatory (ESO) Survey is in the range 7–14 per cent (Merle et al. 2020).

In SB1's, the periodic radial-velocity (RV) variation of the primary/host star is induced by the gravitational influence of its orbiting companion. Unfortunately, stellar activity phenomena (spots, plages, and activity cycles), which affect line profiles may produce a variation in RV that mimics or hides a Keplerian signal resulting from a substellar companion (Queloz et al. 2001; Dumusque et al. 2012; Robertson et al. 2013; Santos et al. 2014). Therefore, the identification of the source of the RV variations is difficult.

Binaries with low velocity amplitude (large mass ratio) help constraining binary formation models. However, the Ninth Catalog of Spectroscopic Binary Orbits (SB9[1]; Pourbaix et al. 2004) does not contain many binaries with primary velocity amplitude lower than $1\,\mathrm{km\,s^{-1}}$: around 0.4 per cent of the catalogue, with a mean mass function value of $6.3 \times 10^{-5}\,\mathrm{M_\odot}$, according to the latest version (2021-03-02). Our analysis can provide them.

We look at well-studied and supposedly stable stars as a validation set to establish the detection thresholds to apply for the detection of spectroscopic multiple stars in our future studies. Indeed, the detection of RV variations depends on the stability of the instrument, the quality of the measured RVs, their derived uncertainties, and time baseline. Therefore, our main aim in this paper is to assess the stability of a sample of RV standard candidates used to calibrate the Radial Velocity Spectrometer (RVS; Cropper et al. 2018) onboard *Gaia* (Gaia Collaboration et al. 2016). To this aim, we systematically apply an efficient procedure that searches for a binary signature in the RVs, even if it is of low amplitude (i.e. in the substellar regime). The criteria to select the *Gaia* RV standard stars and the list of candidates are described in Soubiran et al. (2013, 2018, hereafter CS13 and CS18, respectively). These stars should be stable over at least 300 d and not have any bright neighbours ($\Delta I < 4$ mag) within

★ E-mail: boulkaboulamina@gmail.com (AB); yassine.damerdji@uliege.be (YD); tmorel@uliege.be (TM)
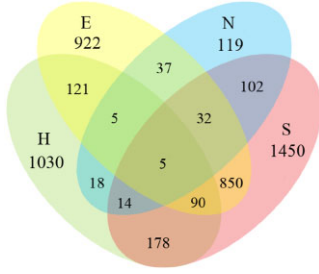
[1]http://sb9.astro.ulb.ac.be

Figure 1. Venn diagram showing the number of stars shared by different instruments: HARPS (H), SOPHIE (S), ELODIE (E), and NARVAL (N).

a circular region of 20 arcsec radius to make sure the RVS spectrum is not contaminated. Their RV scatter (3σ) should not exceed 300 m s^{-1} throughout the duration of the mission (originally planned for 5 yr when it was selected by European Space Agency (ESA), but the mission was extended). The selection of the most stable candidates was performed in advance of the mission, from a compilation of RV measurements from different spectrographs. It implied a necessary compromise between the number of standards needed for the RVS calibrations (several thousands) and the number of stars followed up from the ground over a sufficient time baseline to test their stability. As a consequence, the selected standard stars are only candidates, and some of them revealed variations with a remarkable trend during the *Gaia* observations (CS18). For the target stars, we thus track SB1 systems with long-term RV variations in the catalogue of RV standards for *Gaia* RVS to clean it and improve the calibration of the next releases.

This paper is structured as follows. In Section 2, we give an overview about our target stars; in Section 3, we outline the methodology adopted in the spectroscopic analysis; in Sections 4 and 5, we describe the overall results for the sample; in Section 6, we give details about stars showing trends; in Section 7, we focus on the long-term RV variations and their correlations with different activity indicators and cross-correlation function (CCF) parameters. Finally, we draw our main conclusions in Section 8.

2 THE TARGET STARS

We initially considered the sample of 2351 stars from the catalogue of *Gaia* RV standard star candidates (CS18) with CAL1 quality (wavelength calibrators for DR2 and DR3). The CAL1 stars were chosen to have at least two ground-based RV measurements spread over more than 300 d with a standard deviation of the mean less than 100 m s^{-1}.

The HARPS (High Accuracy Radial velocity Planet Searcher), SOPHIE (Spectrographe pour l'Observation des Phénomènes des Intérieurs stellaires et des Exoplanètes), ELODIE, and NARVAL samples contain 1030, 1450, 922, and 119 stars, respectively. For 11 stars among the HARPS sample, CS18 used CORALIE spectra. Stars in common between different instruments are shown in Fig. 1. We provide an excerpt of the sample in Table 1, which gives the target coordinates (α, δ), visual apparent magnitude V, spectral type, observation duration, signal-to-noise ratio (S/N) range, the number of observations before and after outlier filtering (Section 5), as well as the instrument used.

The archive spectra we analysed are available in the ESO data base archive for HARPS[2] and in the relevant instrument website for

SOPHIE,[3] ELODIE[4] (Moultaka et al. 2004), and NARVAL[5] (Donati et al. 1997), (Petit et al. 2014). As recent HARPS, NARVAL, and SO-PHIE observations are available, we benefit from more measurements than in CS18 and, thus, also from a longer time span. These additional spectra have been retrieved through queries to ESO, NARVAL, and SOPHIE archives. The number of these additional spectra for each target is listed in Table 1. Taking these additional data into account increases the total number of spectra by 19.5 per cent, 11.8 per cent, 38.2 per cent, and 74.8 per cent for NARVAL, ELODIE, SOPHIE, and HARPS, respectively. The additional ELODIE spectra are those removed from CS13 and CS18; they either have low S/N value or do not have archival RVs. We filtered out those with low S/N when analysing the RVs.

HARPS spectra have a resolving power of $R = \lambda/\Delta\lambda = 115\,000$ covering a wavelength range of 3780–6910 Å, while SOPHIE achieves $R = 75\,000$ and covers the wavelength range 3872–6943 Å. ELODIE, on the other hand, covers the wavelength range 3850–6800 Å with a spectral resolution of 42 000. Covering the optical range 3700–10 000 Å, NARVAL has $R \sim 81\,000$.

3 METHODS

We developed a pipeline different from the instrument ones to derive the RVs based on a synthetic spectrum and initial stellar parameters rather than on numerical masks. We simultaneously derive the RV and the line broadening (vbroad: which makes no distinction between rotation and macroturbulence velocities) using the minimum distance algorithm based on the minimization of the quadratic sum, χ^2, of the difference between the observed spectrum and synthetic spectra (theoretical template). We vary as free parameters: the effective temperature, $T_{\rm eff}$, surface gravity, log g, total line broadening, vbroad, metallicity, [Fe/H], and abundance ratio of the α-process elements, [α/Fe]. The minimum χ^2 gives the template that best matches the observed spectrum. This procedure is similar to that adopted for the ground-based processing of the *Gaia* RVS spectra (Sartoretti et al. 2018).

The template is a synthetic spectrum $s(\lambda_{\rm s})$ resampled to the observations, as indicated in equation (1) (David et al. 2014), where $\lambda_{\rm s}$ is the rest-frame wavelength scale and G is Green's function convolved with a Gaussian kernel. In order to have the template and observed spectra fully overlapping in wavelength space after applying the Doppler shift, the wavelength range of the former must extend beyond the observed one (David et al. 2014). It is then convolved with the rotation profile u[vbroad] given by Gray (2021). We thus have

$$T(\lambda, {\rm RV}, {\rm vbroad}) = u[{\rm vbroad}] * G\left[\lambda, \lambda_{\rm s}\left(1 + \frac{{\rm RV}}{c}\right)\right] * s(\lambda_{\rm s}).$$
(1)

We minimize the quadratic sum over each wavelength element

$$\chi^2 = \sum_i w_i (S_i - T_i')^2$$
(2)

$$T_i' = P_n(\lambda_i)\, T(\lambda_i, {\rm RV}, {\rm vbroad}) + b\,,$$
(3)

where S_i is the observed spectrum, w_i is the statistical weight, and T_i' is the single-lined model given by equation (3). $P_n(\lambda)$ is the polynomial modelling the continuum as a function of wavelength, λ. T is the normalized synthetic spectrum used. It is convolved with the instrument line-spread function assumed to be Gaussian, then

[3]http://atlas.obs-hp.fr/sophie/
[4]http://atlas.obs-hp.fr/elodie/index.html
[5]http://polarbase.irap.omp.eu/

Table 1. List of targets: target ID, coordinates (α, δ) at the specific epoch, visual apparent magnitude, V, spectral type taken from CS18, SpT, total time span, T, minimum and maximum S/N values, total number of analysed spectra, N_{init}, the final number of measurements after filtering, N, the number of additional spectra compared to CS18, N_{add}, and the instrument used.

HIP/TYC	α (°)	δ (°)	Epoch	V (mag)	SpT	T (d)	min(S/N)	max(S/N)	N_{init}	N	N_{add}	Instrument
47	0.135	−56.836	J2015.5	10.75	K3V	6154.04	23.5	44.7	10	10	3	H
57	0.168	−69.676	J2000.0	8.24	K1V	4766.05	42.4	143.0	38	37	3	H
80	0.245	−11.824	J2015.5	9.11	G2V	4266.28	40.7	158.2	124	121	86	H
142	0.454	66.306	J2015.5	7.32	K0	1473.00	43.3	133.0	32	32	1	S
184	0.590	11.006	J2015.5	8.47	K0V	0.00	59.3	59.3	1	1	0	E
184	0.590	11.006	J2015.5	8.47	K0V	4035.58	43.8	81.8	5	5	1	S
348	1.091	12.958	J2015.5	8.64	G5	3273.99	40.4	60.7	4	4	0	S
400	1.236	23.270	J2015.5	7.81	G9V	5096.60	27.3	195.1	348	346	297	S
413	1.262	−36.015	J2015.5	7.74	G0V	5739.22	26.0	131.8	18	18	7	H
436	1.322	−67.835	J2015.5	8.49	K4.5V	6229.99	32.4	127.4	82	80	69	H
...												

This table is available in its entirety online at the CDS. A portion is shown here for guidance regarding its form and content.

with the rotational broadening profile, and finally Doppler shifted. *b* refers to the background flux. Even though macroturbulent velocity has an effect on the line shape distinct from that from rotation, we only considered the rotational profile. The vbroad parameter, thus, includes both effects.

The grid of synthetic spectra, T ($R > 150\,000$), is extracted from the POLLUX data base (Palacios et al. 2010). We chose the MARCS (Gustafsson et al. 2008)-AMBRE (De Laverny et al. 2012) plane-parallel and spherical atmosphere models with a microturbulent velocity (1 km s^{-1} for the former grid and either 1 or 2 km s^{-1} for the latter) that is suitable to cool stars in the range 3500–8000 K. Because they are also adopted for the ground-based processing of the *Gaia* RVS data (Sartoretti et al. 2018), we preferred the MARCS-AMBRE synthetic spectra over the PHOENIX ones (Husser et al. 2013).

The astrophysical parameters (APs: T_{eff}, log g, [Fe/H], and [α/Fe]) of the template that best matches our target spectrum are derived by using a minimum distance algorithm. A first guess of the RV and vbroad is derived by a least-squares fitting method in Fourier space to find an approximate solution for each spectrum. The solution is refined afterwards by Levenberg–Marquardt minimization (Press et al. 1986, section 15.5.2). More details about this method can be found in section 7.5 of Sartoretti et al. (2018).

The line broadening is considered a non-linear parameter, which is required to be the same for all spectra of a given target. We initially fit each spectrum individually, allowing us to exclude spectra with an outlying χ^2 (outside the range median$\pm 5\sigma$) from the subsequent global fit, in which we measure a common vbroad for all spectra. Then, we fix vbroad and remeasure the RVs to obtain non-correlated values.

The RVs estimated using this method should be more homogeneous than archival pipeline RVs that are occasionally based on an unsuitable numerical correlation mask or on different masks for the same star. As an example, choosing either a K5 or a G2 mask induces an RV shift reaching up to 20 m s^{-1} (Anglada-Escudé & Butler 2012).

We fitted the observed spectra within the five spectral ranges: 4000–4300, 4400–4800, 4900–5200, 5400–5800, and 6000–6200 Å. These spectral domains present the advantage of not being contaminated with telluric lines. We also excluded the Balmer lines that would hinder the RV measurement, except the Hδ line because it is weak.

We looped over MARCS-AMBRE plane-parallel and spherical synthetic spectra with microturbulence velocity of 1 and 2 km s^{-1}; for APs initially ranging from [$p - \Delta p$] to [$p + \Delta p$] with p referring to the AP: either T_{eff}, log g, or [Fe/H] whose initial estimates are extracted from the most recent estimates in the PASTEL catalogue

(Soubiran et al. 2016). The parameters are taken from *Gaia* DR2 (Gaia Collaboration et al. 2018) for the 13 stars not included in PASTEL. The parameter steps, Δp, are $\Delta T_{\mathrm{eff}} = 250$ K, Δ log $g = 0.5$ dex, and Δ[Fe/H] $= 0.25$ dex, while we consider all possible [α/Fe] for every combination. If one of the determined parameters is on the interval edge, $p_0 = [p \pm \Delta p]$, the template parameters for the second iteration lie in the interval [p, $p + 2\Delta p$] or [$p - 2\Delta p$, p]. This process is repeated until the parameter is at the centre of the box. We find the best template for each domain separately, then we choose the one that yields the minimum χ^2 sum for all domains. We do not fit the domains simultaneously, as there is a shift reaching 100 m s^{-1} between the RVs estimated for each of them (as detailed in the following section).

The polynomial degree of the continuum function in each interval is chosen using an F-test, which compares successive polynomial models fitting residuals with a degree starting from 3 and reaching up to 10 to identify the polynomial of the lowest degree that yields an acceptable solution.

As the flux errors are not provided by the HARPS pipeline, we have opted for the unit weighting: $w_i = 1/\sigma_i^2$, with $\sigma_i = 1$ and $w_i = 1$. For consistency, it was also the case for the spectra obtained with other spectrographs. The Poisson weighting ($\sigma_F = \sqrt{F}$, where F is the flux expressed in photon counts) accounts for the loss in RV measurement precision as the broad and deep spectral lines broaden the χ^2 function. The χ^2 was rescaled for each spectrum in order to obtain normalized flux residuals ($S - T'$) with unit variance (Andrae, Schulze-Hartung & Melchior 2010). There is no need to rescale if the flux residuals are good enough (i.e. according to Anderson–Darling normality test; Anderson & Darling 1952). Great care is taken to standardize input fluxes when applying unit weight scheme.

Our vbroad is a measure of the line broadening arising from rotation and macroturbulence after accounting for the effect of microturbulence and instrumental resolution. Since vbroad depends on APs, we adopted as uncertainty the standard deviation of measurements obtained for synthetic spectra with parameters [$p \pm \Delta p$]. Namely, we compared vbroad of the best-fitting synthetic spectrum and that obtained for closely similar stellar parameters (T_{eff}, log g, and [Fe/H]).

4 ANALYSIS OF THE FULL SAMPLE

4.1 RV offset and vbroad analysis

We measured the RV and vbroad of 2351 stars by fitting HARPS/SOPHIE/ELODIE/NARVAL spectra with MARCS-
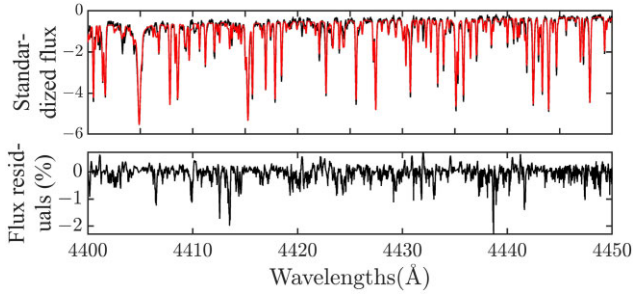
Figure 2. Top panel: HIP21821 best fit with MARCS-AMBRE synthetic spectrum for observation BJD = 2455493.8 in the interval 4400–4450 Å with RV = 9.0782 ± 0.0057 km s^{-1} and vbroad = 4.79 ± 0.26 km s^{-1}. Observed spectrum in black and synthetic spectrum in red ($T_{\rm eff}$ = 6000 K, log g = 4.0 dex, [Fe/H] = -0.5 dex, and [α/Fe] = 0.2 dex). The fit residuals divided by the standardized flux in that domain are shown in the bottom panel.

AMBRE synthetic spectra. HARPS, then SOPHIE if not available, spectra were always preferred to select the best synthetic spectrum used to estimate the two quantities.

An example of our fitted spectrum along with the fit residuals is shown in Fig. 2 for HIP21821 in the range 4400–4450 Å. It can be seen that the fit is globally good, except for a few weak lines. This could be due to template mismatch and the fact that the line list adopted to compute the synthetic spectrum is necessarily imperfect.

The APs of the best synthetic spectra selected after the minimization are listed for a portion of the sample in Table 2. We computed $\triangle$AP, which is the difference between the AP of the best template and that selected in PASTEL. We plot $\Delta \log g$ as a function of $\Delta T_{\rm eff}$ in the bottom right-hand panel of Fig. 3 where the colour bar denotes Δ[Fe/H]. The trend stars (detailed in the next section) are plotted as diamonds. The distribution of $\Delta T_{\rm eff}$ is shown in the top right-hand panel, where 92.9 per cent of the stars have $|\Delta T_{\rm eff}| \leq 250$ K, while 90.1 per cent of the stars have $|\Delta \log g| \leq 0.5$ dex, as shown in the distribution in the bottom left-hand panel. We have 86.3 per cent of the targets with APs inside the box [± 250 K, ± 0.5 dex]. The rate drops to 68.1 per cent if we include those with $|\Delta$[Fe/H]$| \leq$ 0.25. We show in Fig. 4 the distribution of the difference in RVs estimated using the best template and that with APs closest to those in PASTEL. The median is 5.30 ± 0.02 m s^{-1}. The multiple modes present in the distribution could be related to whether all APs or just one of them differ between the two templates. Even though the shift would not affect the orbital solutions in case of RV variations of high amplitude, it could induce a difference for lower-amplitude systems.

This is expected as the shift between HARPS pre- and post-fibre-upgrade RVs is temperature dependent, as discussed below.

We compare in Fig. 5 the difference between our measured RVs, RV$_m$, and those extracted from instrument archive, RV$_s$, as a function of RV$_s$. For HARPS (top panel), the difference between measured and archived RVs is -241.70 ± 2.09 m s^{-1} for the M2 numerical mask, while it is 201.40 ± 2.09 and 228.90 ± 0.07 m s^{-1} for the K5 and G2 masks, respectively. In the same way, we compare the RV measurements from SOPHIE spectra in Fig. 5(b). The shift is close to the HARPS one with positive offsets of 217.8 ± 0.3, 228 ± 48, 252.4 ± 0.9, and 265 ± 5 m s^{-1} for the K5, K0, G2, and F0 masks, respectively. ELODIE has the largest shifts: 336.4 ± 0.8 and 282 ± 4 m s^{-1} for the K0 and F0 masks, respectively. Finally, the shift for NARVAL is 157 ± 3 m s^{-1} for the only mask used, G2.

Some archive HARPS RVs have been estimated using different masks for the same spectrum. For the same date, the median of the difference between RVs measured using either an M2 or a K5 mask is 439.1 ± 2.0 m s^{-1}, which is very similar to the difference between the shifts RV$_s$ − RV$_m$ for the M2 and K5 masks: 443.1 ± 2.1 m s^{-1}. Therefore, we conclude that our measurements are more consistent and that the archived RVs obtained from M2 masks are overestimated.

The average offset between our measurements and those of the archives is 240.4 m s^{-1} considering all spectrographs. This offset is caused by the difference in instrument RV zero-points and the method used. Frémat et al. (2017) found a similar shift of 220 ± 30 m s^{-1} between their UVES (Ultraviolet and Visual Echelle Spectrograph) measurements and those found in the CS13 catalogue. We list in Table 2 the mean of our measured RVs, $\langle$RV$_m\rangle$, and the median given by CS18, $\langle$RV$_{\rm CS18}\rangle$.

The mean shift between the RVs obtained for the reference domain 4400–4800 Å and the four others is around 40 m s^{-1}, except for 4900–5200 Å where it is 200 m s^{-1} and can occasionally reach up to 2 km s^{-1}. We plot the shift for the four domains as a function of $T_{\rm eff}$ in Fig. 6. We attribute the temperature and wavelength dependences of the shift to template mismatches, as well as to the instrumental calibration.

Furthermore, the HARPS fibre has been upgraded in 2015 June, which caused an offset in the RV measurements compared to pre-upgrade observations. According to Lo Curto et al. (2015), the RVs are correlated with the width of the spectral lines and the shift depends on the spectral type. As we have noticed that the recovery rate of known planetary periods depends on the shift, we decided to fit the shift as a function of $T_{\rm eff}$ by maximizing the number of known periods recovered (see the next section). We obtain RV$_{\rm postUpgradeCorrected}$ = RV$_{\rm postUpgrade}$ − $2.0 \times 10^{-3} T_{\rm eff}$(Template) (K) + 7.3 m s^{-1}. Fig. 7

Table 2. Stellar parameters of the best-fitting synthetic spectra ($T_{\rm eff}$, log g, [Fe/H], and [α/Fe]), along with vbroad, our mean measured RV, $\langle$RV$_m\rangle$, and the median RV from CS18, $\langle$RV$_{\rm CS18}\rangle$. A vbroad value of 1.91 km s^{-1} is the lowest limit that can be measured by our algorithm.

HIP/TYC	$T_{\rm eff}$ (K)	log g (dex)	[Fe/H] (dex)	[α/Fe] (dex)	vbroad (km s^{-1})	$\langle$RV$_m\rangle$ (km s^{-1})	$\langle$RV$_{\rm CS18}\rangle$ (km s^{-1})	Instrument
47	4750	5.0	-0.25	0.1	$<1.91 \pm 1.28$	12.022 ± 0.003	11.752 ± 0.001	H
57	5500	5.0	0.00	0.2	3.52 ± 0.50	37.137 ± 0.001	36.851 ± 0.0004	H
80	5750	4.0	-0.75	0.3	3.63 ± 0.45	-11.063 ± 0.001	-11.365 ± 0.001	H
142	5750	4.0	0.25	-0.2	4.77 ± 0.42	-21.458 ± 0.002	-21.721 ± 0.002	S
184	5250	4.5	0.00	0.0	1.98 ± 1.11	-17.245 ± 0.005	-17.512 ± 0.002	S
184	5250	4.5	0.00	0.0	3.00 ± 1.11	-17.217 ± 0.028	-17.512 ± 0.002	E
348	6000	4.5	-0.25	0.1	3.52 ± 0.67	18.877 ± 0.005	18.587 ± 0.003	S
400	5250	4.5	-0.50	0.2	$<1.91 \pm 1.32$	7.8440 ± 0.0003	7.577 ± 0.001	S
413	6250	4.5	-0.25	0.1	5.01 ± 0.47	4.829 ± 0.002	4.525 ± 0.001	H
436	4750	5.0	-0.50	0.2	$<1.91 \pm 0.44$	40.516 ± 0.001	40.228 ± 0.0004	H
...								

This table is available in its entirety online at the CDS. A portion is shown here for guidance regarding its form and content.
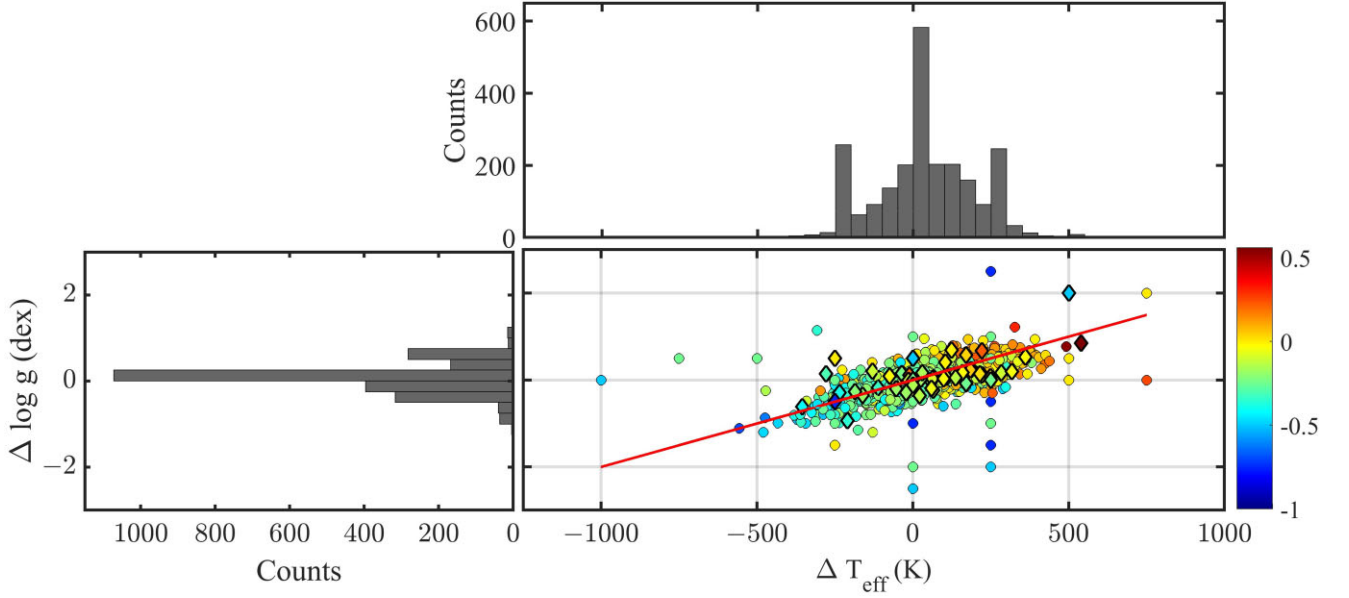
Figure 3. Top panel: distribution of the differences between the best template and PASTEL's T_{eff}, ΔT_{eff}. Bottom left-hand panel: $\Delta \log g$ distribution. Bottom right-hand panel: $\Delta \log g$ as a function of ΔT_{eff} where the trend stars (see the next section) are plotted as diamonds. The colour bar denotes Δ[Fe/H]. The red line shows the relation $\Delta \log g = \Delta T_{eff}/500$.
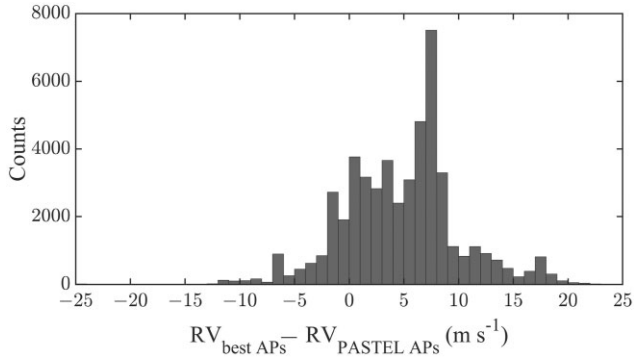

Figure 4. Distribution of the difference in RVs estimated from the best-fitting and PASTEL templates with a median of $5.30 \pm 0.02\,\mathrm{m\,s^{-1}}$.

shows an example of the corrected RV time series in the range 4400–4800 Å, where the HARPS post-upgrade measurements are plotted in red.

Applying the public SpEctrum Radial Velocity AnaLyser (SERVAL) pipeline to HARPS spectra, Trifonov et al. (2020, hereafter T20) computed RVs based on the χ^2 minimization where the template is created by shifting and co-adding all individual spectra of the target. Thus, they derived differential (relative) RV values. We fit our measured RVs to theirs using orthogonal regression (Krystek & Anton 2007) and list the slope and Y-intercept of each target in Table 3 for pre- and post-upgrade measurements, respectively. These coefficients are estimated only for targets with more than three measurements. We show in Fig. 8 the distribution of the estimated slopes with overplotted normal distribution $\mathcal{N}(0, 1)$. The asymmetry is mainly due to the small uncertainties of T20 compared to ours. In addition, there are 10 stars with $(\text{Slope} - 1)/\sigma_{slope} \leq -5$. The lowest value is for HIP21821: Its fitted spectrum is shown in Fig. 2 for the domain 4400–4450 Å. We compare our measured RVs, those derived by the HARPS pipeline, and those of T20 in Fig. 9. We find a linear relation between our RVs and those from the HARPS pipeline with a

slope of 0.99 ± 0.16. The deviation from the 1:1 relation with respect to T20 RVs could either be due to the nightly zero-point corrections they applied to their RVs or for not taking into account the difference in RVs between different domains.

Even though our measurements are less precise than T20's as we used portions of the spectrum, the difference in RVs between these portions is taken into consideration. In addition, these RVs are measured as absolute values with a shift around $200\,\mathrm{m\,s^{-1}}$ compared to pipeline's RVs and show more homogeneity. On the other hand, T20 velocities are template free and therefore do not suffer from template mismatch problems.

We plot in Fig. 10 the histogram of the normalized residuals of vbroad for 1354 stars obtained by comparing our measurements and $V \sin i$'s taken from the literature (Glebocki & Gnacinski 2005, hereafter GGS). The differences were divided by our uncertainties as GGS's catalogue does not provide uncertainties for all estimations. We overplot the distribution for slow and fast rotators: $V \sin i$(GGS) below and above $4\,\mathrm{km\,s^{-1}}$. The precision of the measurements is expected to decrease when the true value is of the same order as or lower than the instrumental resolution ($\sim 2.6\,\mathrm{km\,s^{-1}}$). Therefore, the histogram exhibits a clear asymmetry at low $V \sin i$ values indicating that our vbroad might be overestimated in this case. On the other hand, we note that a large fraction of the measurements found in GGS are taken from Nordström et al. (1997), where they have been rounded off differently depending on $V \sin i$. Some of the structures in the right wing of both distributions were found to be linked to this rounding.

4.2 RV zero-point between instruments

As there are stars observed with several instruments (Fig. 1), each of those having their own reduction pipeline and method for deriving the RVs, we must determine their relative RV offset. For all instruments, we adopted the HARPS RV reference frame. In Table 4, we compare the offset between different instruments with respect to CS13's estimates. For all masks of a given instrument, we first estimate
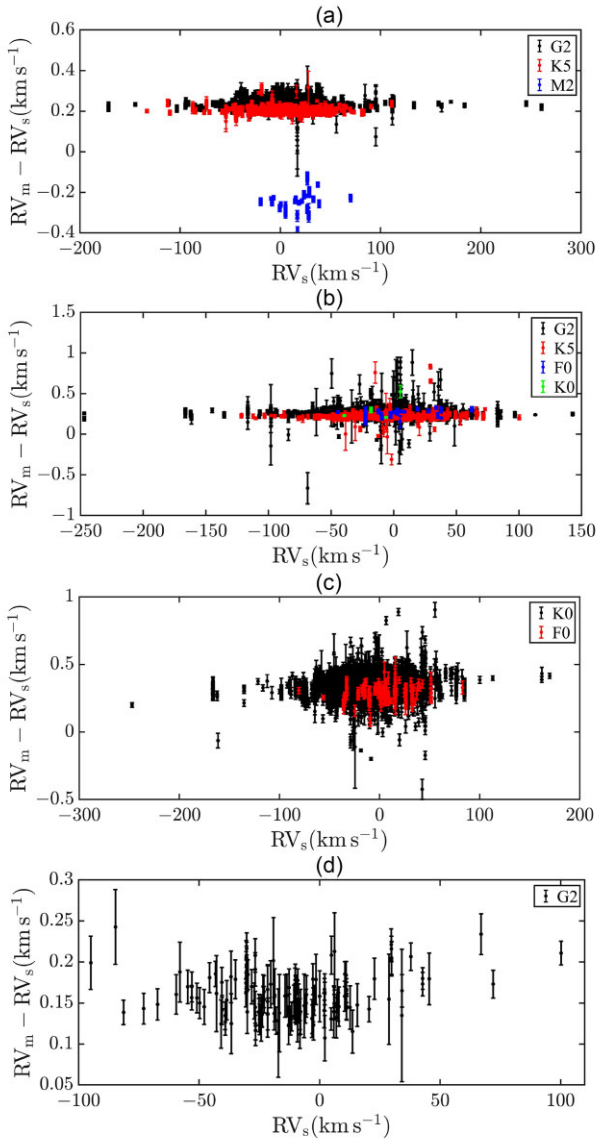
Figure 5. Difference between our measured RVs, RV_m, and those extracted from the instrument pipeline, RV_s, as a function of RV_s. From top to bottom: (a) HARPS, (b) SOPHIE, (c) ELODIE, and (d) NARVAL. The shift is around $300 \, \mathrm{m \, s^{-1}}$ for ELODIE and $200 \, \mathrm{m \, s^{-1}}$ for the other three instruments. It is true for all masks except for the M2 mask (see the upper panel) for which we argue that the RVs in the archives are overestimated.

the median shift between measured and archived RVs. The offset is the difference between the shifts for the two instruments considered. The offset for HARPS versus SOPHIE is equal within uncertainties to the one estimated by CS13, but it is much more precise. The agreement for NARVAL is less satisfactory because of the different wavelength calibration methods, although it remains within 3σ. We follow CS13 in fitting the offset between ELODIE and other instruments as a function of the $B - V$ colour index. The shift between RVs extracted from the instrument pipeline and our measurements as a function of $B - V$ for SOPHIE, ELODIE, and HARPS is given by $(88.3 \pm 0.6) \, (B - V) - (304.7 \pm 0.4)$, $(-175.1 \pm 2.7) \, (B - V) - (213.4 \pm 1.8)$, and $(66.7 \pm 0.2) \, (B - V) - (271.3 \pm 0.1) \, \mathrm{m \, s^{-1}}$, respectively. The offset between ELODIE and SOPHIE as a function of the colour index is $(-263.4 \pm 2.7) \, (B - V) + (91.4 \pm 1.8) \, \mathrm{m \, s^{-1}}$.

The slope is close to the one found by CS13: $-259 \, \mathrm{m \, s^{-1}}$. The offset between HARPS and ELODIE as a function of $B - V$ is thus $(241.8 \pm 2.7) \, (B - V) - (57.9 \pm 1.8) \, \mathrm{m \, s^{-1}}$.

The offset between instruments has also been carefully taken into account in CS18, when all the measurements were put into the SOPHIE system. Since the shift between our measured and archived RVs is coherent for different instruments, we adopted the RVs obtained from 4400–4800 Å as our reference in the following.

5 ORBITAL SOLUTIONS

In order to confirm the stability of the targets with at least 10 observations, we searched for high level of RV variability caused by possible companions. In the search for orbital parameters, we analysed the flux residuals $(S - T^i)$ of each fit and determined their standard deviation and normalized bias (bias $=$ median$/\sigma_{\mathrm{median}}$). We filtered out the RVs based on these two metrics using a median absolute deviation filter. The RVs are the weighted mean value for the five wavelength ranges, where we considered the domain 4400–4800 Å as the reference one and corrected the RVs from the other domains by subtracting the median of the shift. This procedure allows us to exclude outliers. For specific dates, we also omitted RV measurements that have a large drift in the pipeline wavelength calibration.

We applied the Heck, Manfroid & Mersch (1985) periodogram (hereafter HMM), as revisited in Zechmeister & Kürster (2009), to the RV data set in order to perform a period search. To assign a false alarm probability (FAP) to peaks in the periodogram, we constructed an empirical cumulative probability distribution function from the highest peaks of 10^6 realizations of white noise periodograms with the same time sampling. At first, we fitted the data by a trend with a maximum polynomial degree equal to 3. We considered as significant peaks in the frequency periodograms those that are above a probability threshold of 95 per cent. These are then used as an input in a Zechmeister & Kürster Keplerian periodogram to find a first guess of the other orbital parameters. The trend is taken into account (subtracted) if the period of the highest peak in the periodogram exceeds the total time span. The period search process is repeated until there are no peaks exceeding the probability threshold in the HMM periodogram. It is an iterative procedure, where the best solution is successively subtracted to search for significant periodic signals in the residuals, similarly to the method described in Gosset et al. (2001). A global fit taking into account all the solutions derived during the previous steps is applied and RV residuals are then reanalysed in the next iteration. Then, we refined the solutions of all peaks above the significance level simultaneously. In the case of a singular algebraic system, the fit was constrained to a circular orbit (e and ω fixed to zero). The uncertainties in the orbital parameters are obtained from the variance–covariance matrix (Press et al. 1986, section 15.4.1). In order to avoid the 1 d period alias, we searched for periods longer than 2 d. The codes, developed in MATLAB (MATLAB 2022) and JAVA Open JDK, are a generalization to a multiperiodic fit of those to produce the *Gaia* DR3 SB1 catalogue (Gosset et al., in preparation).

We note that our approach includes some approximations. We considered all periodogram's peaks that are higher than FAP even though the test is only suitable for the highest one. In addition, a fitted curve subtraction introduces some correlations in the residuals that we have neglected by applying the same FAP to all the levels of time series.
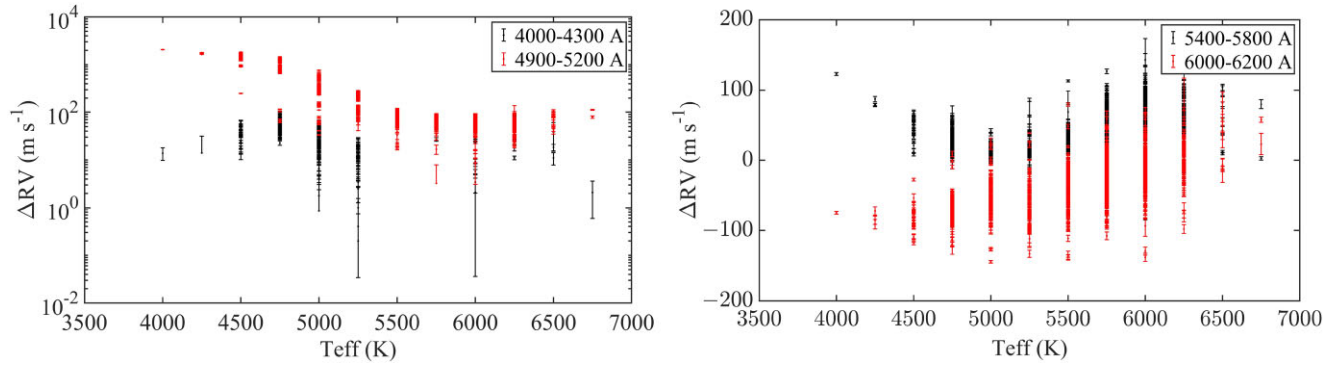
Figure 6. Variation of the RV offset of HARPS targets with respect to that for the wavelength domain 4400–4800 Å for the four other spectral regions: 4000–4300 and 4900–5200 Å (left-hand panel), and 5400–5800 and 6000–6200 Å (right-hand panel). The data are shown as a function of T_{eff}.
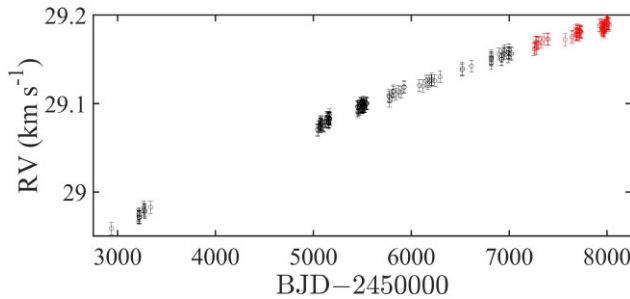

Figure 7. RV variation for HIP 1444 obtained from fitting the interval 4400–4800 Å. HARPS fibre post-upgrade measurements are plotted in red. The RVs exhibit a trend variation with an amplitude of 233.6 m s^{-1}.
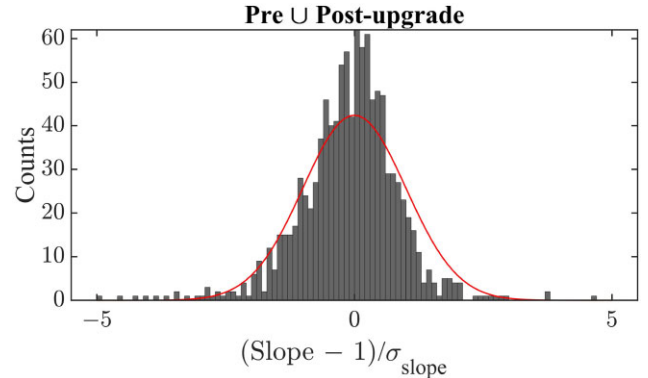

Figure 8. Distribution of the normalized and zero centred orthogonal regression slope between our measured and T20 HARPS RVs (Pre- ∪ Post-upgrade). The normal distribution is overplotted in red.

A total of 134 targets already have an orbital solution in the literature (190 systems). The known-period success rate with PASTEL template APs (71.6 per cent) is lower than with our pipeline best template APs (72.6 per cent) where the HARPS pre-/post-fibre-upgrade measurements are treated separately.

Among the stars with an orbital solution from HARPS, six have an RV amplitude close to or exceeding the *Gaia* RV variability limit (i.e. 300 m s^{-1}): HIP1692, HIP26394, HIP36941, HIP62534, HIP71001, and HIP113834. However, only HIP26394, HIP71001, and HIP113834 exceed the stability level ($3\,\sigma_{\mathrm{RV}} = 300$ m s^{-1}) as defined in CS13. Among SOPHIE stars, HIP30057 has a scatter exceeding the CS13 stability level ($\sigma_{\mathrm{CS13}} = 106.7$ m s^{-1}).

Estimating the total standard deviation, σ_{Model}, of the orbital model (including all orbital solutions and trends), the follow-

ing stars from the HARPS sample have $\sigma_{\mathrm{Model}} \geq 100$ m s^{-1}: HIP5806 (117.6 m s^{-1}), HIP26394 (105.4 m s^{-1}), HIP62534 (113.9 m s^{-1}), HIP71001 (4694.1 m s^{-1}), HIP108095 (159.6 m s^{-1}), and HIP113834 (164.7 m s^{-1}). For SOPHIE, the stars are HIP115714 (117.7 m s^{-1}) and TYC3239-00992-1 (105.7 m s^{-1}). The scatter of the model for HIP30057 (96.6 m s^{-1}) does not exceed the threshold. The orbital solutions of these Keplerian signals are listed in Table 5 where we were able to recover the known periods for five stars.

However, the estimated period of TYC3239-00992-1 does not match within 5σ the known transit period of 3.852985 ± 0.000005 d (Noyes et al. 2008). We plot the phase-folded RV curve assuming

Table 3. Orthogonal regression coefficients of the fit between our measured and T20 RVs.

HIP/TYC	Slope pre-upgrade	Y-intercept pre-upgrade (km s^{-1})	Slope post-upgrade	Y-intercept post-upgrade (km s^{-1})
47	1.1 ± 1.1	12.022 ± 0.003	–	–
57	0.925 ± 0.085	37.138 ± 0.001	–	–
80	1.57 ± 0.29	− 11.063 ± 0.001	–	–
413	1.68 ± 0.50	4.829 ± 0.002	–	–
436	1.08 ± 0.71	40.518 ± 0.001	1.0 ± 1.1	40.576 ± 0.046
459	1.27 ± 0.17	7.126 ± 0.002	–	–
490	0.881 ± 0.084	2.419 ± 0.004	0.87 ± 0.12	2.481 ± 0.005
569	0.42 ± 0.48	− 27.367 ± 0.001	0.6 ± 1.8	−27.345 ± 0.002
616	0.3 ± 1.1	− 42.777 ± 0.001	–	–
726	0.95 ± 0.10	− 19.090 ± 0.001	1.01 ± 0.24	−19.092 ± 0.002
...				

This table is available in its entirety online at the CDS. A portion is shown here for guidance regarding its form and content.
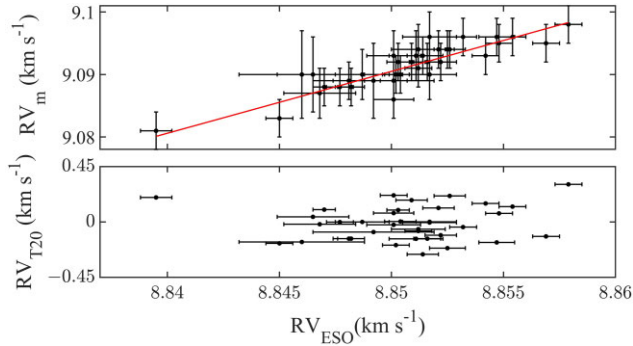
Figure 9. Top panel: HIP21821 measured RVs as a function of those derived by the HARPS pipeline with a slope of 0.99 ± 0.16. Bottom panel: T20 RVs as a function of HARPS pipeline RVs with a slope of 317 ± 113.
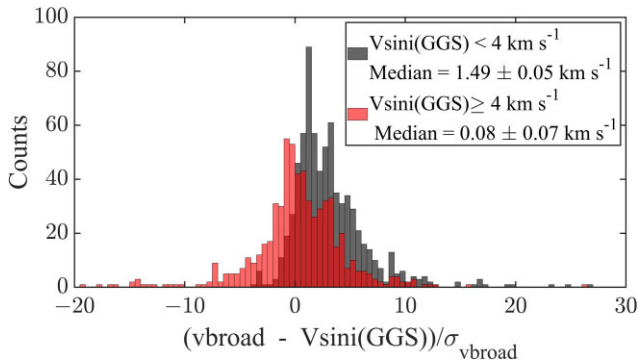

Figure 10. Distribution of the vbroad residuals, [Vbroad $-$ $V \sin i$ (GGS)]$/\sigma_{\mathrm{vbroad}}$, for 1354 stars. There are two histograms: for $V \sin i$(GGS) $\geqslant 4 \,\mathrm{km\,s}^{-1}$ (red) and $V \sin i$(GGS) $< 4 \,\mathrm{km\,s}^{-1}$ (black). Our measured vbroad are overestimated with respect to GGS's for low $V \sin i$ values, as revealed by the asymmetry.

Table 4. RV offsets between instruments (HARPS, SOPHIE, and NARVAL) for all stars compared to those estimated by CS13.

Instruments	Offset (m s^{-1})	
	This work	CS13
HARPS–SOPHIE	20.4 ± 0.3	17 ± 5
HARPS–NARVAL	68.10 ± 2.7	43 ± 7.96

this period in Fig. 11. We were not able to retrieve this period because of the bad sampling and missing data points.

We show HIP26394 and HIP113834 periodograms and orbital solutions in Figs 12 and 13, respectively. The *F* statistic denotes the ratio of two independent χ^2 values (*F* statistic of the pure sine model with respect to the variance), defined as *z* variable from equation (23) of Zechmeister & Kürster (2009).

In addition to the known period of HIP5806, we find two new ones that need to be confirmed. The short period of HIP108095 has not been detected previously and thus it could indicate the presence of a new substellar companion in addition to a second degree trend caused by a more massive companion. For these two stars, σ_{Model} is dominated by the trend scatter. The periodograms and phase-folded RV curves for these newly discovered periods are shown in Figs A1 and A2, respectively. The long period of HIP71001 has a high uncertainty and its RV semi-amplitude is lower than its uncertainty; thus, we are cautious about this solution.

Additionally, TYC8963-01543-1 does not have a significant period or a trend, but it has $\sigma_{\mathrm{CS13}} = 176.6 \,\mathrm{m\,s}^{-1}$. Its RV curve (Fig. 14) suggests the star to be an SB2. We will analyse it in a future work.

6 ANALYSIS OF STARS WITH RV TREND

Some of the stars with long periods exceeding the observation duration have RV variations with an incomplete orbit or exhibit a polynomial trend. We list those with a mean acceleration (RV amplitude, *A*, divided by the time span, *T*) greater than $10 \,\mathrm{m\,s}^{-1}\,\mathrm{yr}^{-1}$, along with their mean acceleration and trend degree in columns 3 and 4 of Table 6 for HARPS targets. There are four stars with previously detected Keplerian signal(s) for which we find an additional signal manifesting as a trend with an acceleration exceeding our adopted threshold: HIP5806, HIP10278, HIP60689, and HIP89354. These trends indicate the presence of an additional companion with a long period. However, this is not necessarily always the case as such variations may have other origins (see Section 7).

There are stars with a very high acceleration value ($\frac{A}{T} >$ $25 \,\mathrm{m\,s}^{-1}\,\mathrm{yr}^{-1}$) that could exceed the variability threshold that was set by the *Gaia* mission ($300 \,\mathrm{m\,s}^{-1}$ in 10 yr): HIP10278, HIP14596, HIP37233, HIP60689, HIP71001, HIP81533, HIP85158, HIP95849, HIP99385, HIP108095, HIP110156, HIP116374, TYC6792-01746-1, and TYC8681-00611-1. Adopting the constancy criterion of CS13, the following stars are variable: HIP12350, HIP14596, HIP37233, HIP71001, HIP99385, HIP108095, HIP110156, HIP116374, and TYC8681-00611-1; they should be reconsidered in the upcoming *Gaia* data release.

In the case of HIP10278, Rickman et al. (2020) combined CORALIE and HARPS measurements to find $P = 123 \pm 41$ yr. This period is too long to be detected with HARPS measurements, and accordingly we only find a first degree trend as the best fit to the data.

Similarly, we list in Table 7 the stars observed with SOPHIE and ELODIE, having an acceleration greater than the threshold: $10 \,\mathrm{m\,s}^{-1}\,\mathrm{yr}^{-1}$. 13 from SOPHIE exceed $25 \,\mathrm{m\,s}^{-1}\,\mathrm{yr}^{-1}$. Among these stars, HIP26037, HIP29611, HIP71291, and HIP76751 have an amplitude greater than the threshold for stability as defined in CS13. Among ELODIE stars, the following have an acceleration exceeding $25 \,\mathrm{m\,s}^{-1}\,\mathrm{yr}^{-1}$: HIP24205 ($34.0 \,\mathrm{m\,s}^{-1}\,\mathrm{yr}^{-1}$) and HIP61157 ($79.5 \,\mathrm{m\,s}^{-1}\,\mathrm{yr}^{-1}$). The trend detected in ELODIE HIP24205 data is a portion of the full orbit of the known period (2117.3 ± 0.8 d; Bean et al. 2007).

In order to be consistent with the σ_{Model} of stars with orbital solution, we also estimate the standard deviation of the trend model using equation (B1).

The considered stars should have a time span longer than 10 yr. We list those with $\sigma_{\mathrm{Model}} \geq 100 \,\mathrm{m\,s}^{-1}$ over 10 and 12 yr in Table 8. We also list those with a scatter greater than $\geq 100 \,\mathrm{m\,s}^{-1}$ over a time span shorter than 10 yr.

We combine the data for stars in common between HARPS, SOPHIE, and ELODIE, in addition to measurements from HIRES by Butler et al. (2017, hereafter B17). The trend amplitude, acceleration, and degree are listed in Table 9. We also list the shift between instruments. The mean shifts with respect to B17 are much larger because their measurements are mean subtracted. After combination, HIP24205, HIP32906, and HIP74702 do not show a significant trend.

In addition to stars with $\sigma_{\mathrm{Model}} \geq 100 \,\mathrm{m\,s}^{-1}$ for each instrument individually, and after combination of data from several instruments, there are four more stars listed in bold in Table 10 having a high RV model scatter. We show their RV curves in Appendix C.

Table 5. Orbital solutions of stars with RV model scatter exceeding the *Gaia* threshold. The solutions are computed with respect to $(2450000 + 100\,E)$ BJD epochs, where E, the reduced reference epoch, is given in column 2. Periods in bold are those recovered. N denotes the number of data points for each target.

HIP/TYC	E	P (d)	K (m s^{-1})	e	ω (°)	T_p (d)	$M_{\min}$ ($M_{\rm Jup}$)	Instrument	N
5806[a]	53	**1238 ± 14**	57 ± 457	0.85 ± 0.94	− 18 ± 73	1184 ± 55	1.572 ± 13.395	H	131
		806 ± 18	6.1 ± 1.1	0.785 ± 0.063	135 ± 14	516.8 ± 7.7	0.172 ± 0.038		
		51.154 ± 0.047	2.97 ± 0.39	0.21 ± 0.13	− 54 ± 38	19.6 ± 5.0	0.053 ± 0.007		
26394[b]	77	**2092.0 ± 1.7**	197.02 ± 0.66	0.645 ± 0.003	− 32.00 ± 0.43	686.35 ± 0.57	9.222 ± 0.207	H	487
62534[c]	61	**1046.2 ± 1.8**	142.9 ± 2.5	0.221 ± 0.008	77.3 ± 1.8	907.8 ± 4.5	6.033 ± 0.210	H	66
71001	51	5106 ± 1222	723 ± 1044	0.080 ± 0.026	99.3 ± 4.7	2878 ± 659	53 ± 76	H	29
108095	51	8.53127 ± 0.00024	33.6 ± 2.8	0.524 ± 0.057	− 46.1 ± 5.8	1.287 ± 0.079	0.261 ± 0.025	H	34
113834[d]	55	**1302.3 ± 1.5**	235.3 ± 2.2	0.318 ± 0.008	101.3 ± 1.1	539.5 ± 3.6	11.596 ± 0.247	H	28
115714[e]	75	**218.473 ± 0.074**	106.6 ± 1.4	0.429 ± 0.010	− 136.7 ± 1.4	214.31 ± 0.70	2.867 ± 0.290	S	99
3239-00992-1	54	3.09410 ± 0.00021	153 ± 58	0.23 ± 0.22	− 63 ± 26	0.91 ± 0.18	1.208 ± 0.463	S	49

References for literature values.
[a]Wittenmyer et al. (2019)
[b]Venner, Vanderburg & Pearce (2021)
[c]Stassun, Collins & Gaudi (2017)
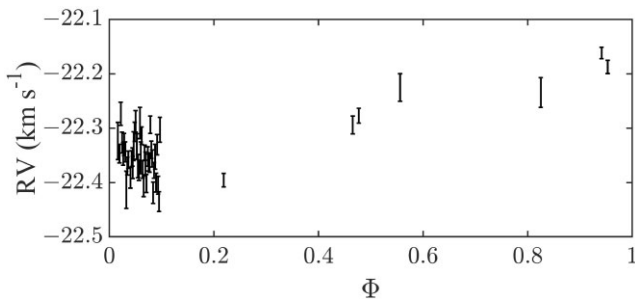[d]Moutou et al. (2011)
[e]Hébrard et al. (2016)

Figure 11. TYC3239-00992-1 phase-folded RV curve with the known period of 3.852985 d. The inhomogeneous phase sampling prevented us to derive this period.

6.1 Stars with companion detected by adaptive optics

The nature of the object causing the trend can be an unseen planetary or stellar companion. Under favourable circumstances in terms of magnitude difference and angular separation, imaging observations can be used to confirm the detection. Some of the trend stars have been observed using adaptive optics (AO). The archive data are provided by NIRC2 (Near InfraRed Camera), NACO (NAOS-CONICA. NAOS; Nasmyth Adaptive Optics System) (Lenzen et al. 2003, Rousset et al. 2003), and SPHERE (Spectro Polarimetric High contrast Exoplanet REsearch) (Beuzit et al. 2010) instruments.

An example of NIRC2 AO image is displayed in Fig. 15 for HIP1444 where the presence of an object at 1.75 ± 0.01 arcsec from the target is revealed. For the 12 stars with available AO images, we calculated absolute magnitudes and projected physical separations using recent distance measurements from Bailer-Jones et al. (2021) based on *Gaia* EDR3. Supposing the system to be physical (i.e. that the companion is at the same distance as the primary), we obtained the absolute magnitudes in the J, H, and K bands. The apparent magnitude of the companion, m_2, is given by $m_1 - m_2 = -2.5\log\frac{f_1}{f_2}$, where m_1 is the apparent magnitude of the primary as given by the SIMBAD data base. For some of these targets, there are objects with unknown parallaxes within a 5 arcsec radius from the sources according to *Gaia* EDR3 (Gaia Collaboration et al. 2021). There may be small differences between the angular separation, θ, from *Gaia* and AO (compare columns 3 and 4 of Table 11) because these measurements were taken at different dates.
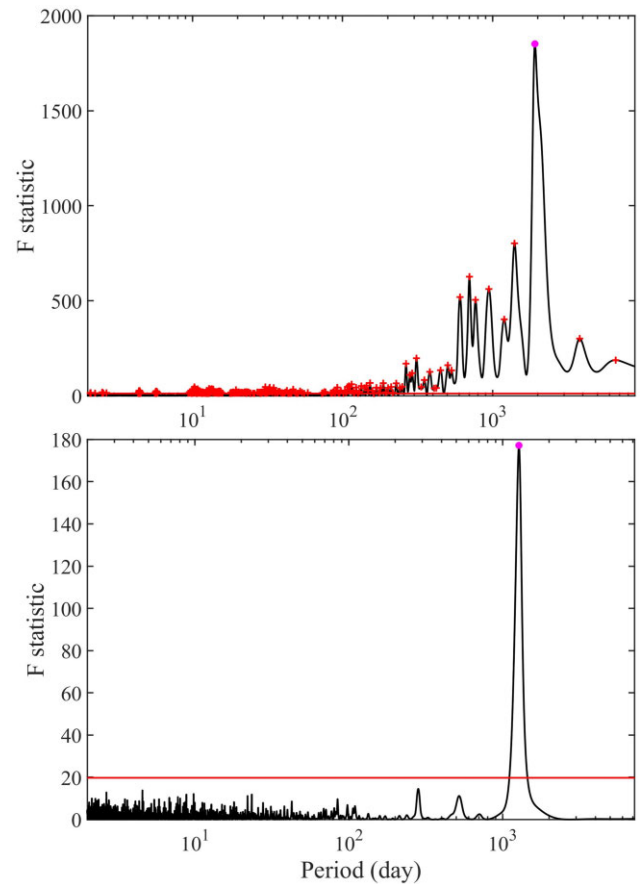

Figure 12. Periodograms for HIP26394 (top panel) and HIP113834 (bottom panel). The red horizontal lines denote the adopted confidence threshold of 95 per cent. Peaks exceeding that threshold are marked by red crosses, while the highest peak is marked in magenta.

The minimum mass of the companion, $M_{\min}$, which can cause a given acceleration, γ_r, is given by (Liu et al. 2002)

$$M_{\min}(M_\odot) = 5.34 \times 10^{-6}(d\,\theta)^2|\gamma_r|\sqrt{27}/2, \qquad (4)$$

where θ is the projected angular separation between the components, $\gamma_r = \frac{dv}{dt}$ is the instantaneous radial acceleration (the derivative of the
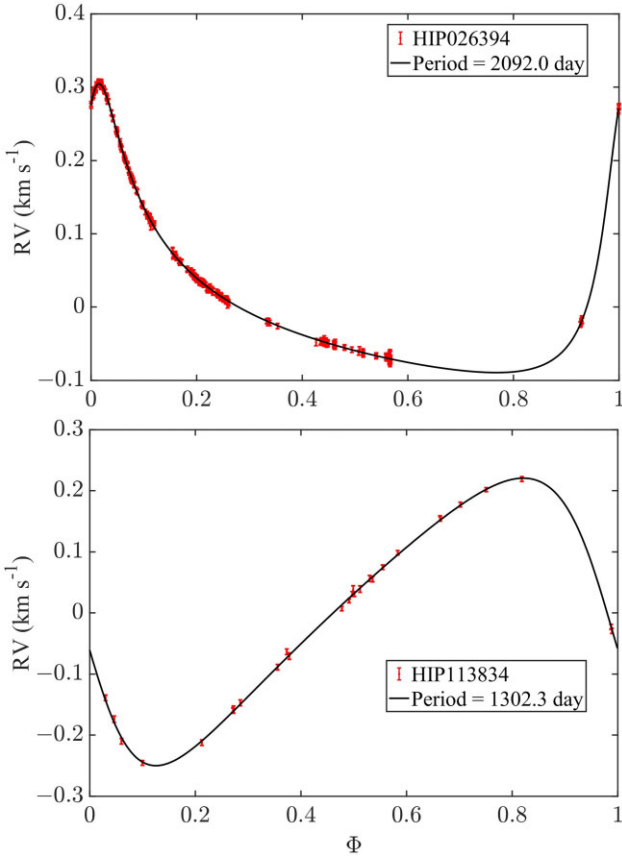
Figure 13. Orbital solutions with semi-amplitude RV exceeding the *Gaia* threshold for HIP26394 (top panel) and HIP113834 (bottom panel) with the periods of 2092.0 ± 1.7 and 1302.3 ± 1.5 d, respectively.
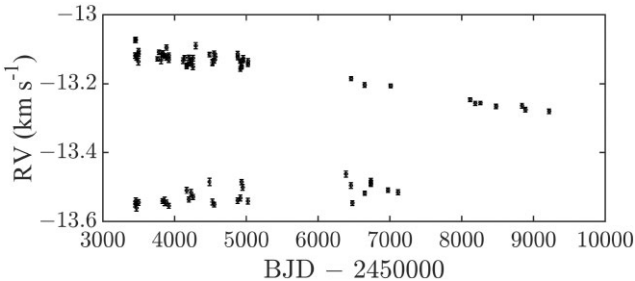

Figure 14. RV variation of TYC8963-01543-1 similar to a trend SB2 where we only measured one RV component.

RV at the mean of dates), and d is the distance to the system. The orbital function $F(i, e, \omega, \phi)$, which depends on the inclination, i, eccentricity, e, longitude of periastron, ω, and orbital phase, ϕ, has a minimum value of $\sqrt{27}/2$ (Torres 1999).

Equation (4) allows us to verify whether the observed trend can be caused by an orbiting body. We estimate the companion photometric mass using the colour–temperature conversions of Pecaut & Mamajek (2013)[6] by matching absolute magnitudes. We list the results of our photometric and astrometric analysis in Table 11, along with

the inferred measurements of physical separations, mass, and period. The period is determined from Kepler's third law with the primary's mass extracted from the literature.

We compare the photometric masses, $M_{\rm phot}$, and the minimum dynamical masses, $M_{\rm min}$, in Fig. 16. If the mass determined from magnitude comparison is smaller than the minimum mass, another companion than the one identified in the AO image is responsible for the RV trend. There are three objects fulfilling this condition: HIP52720, HIP102580, and HIP105606. Therefore, the companion detected by AO is not responsible for the RV acceleration that might be caused instead by an unresolved tertiary companion. For HIP105606, *Gaia* EDR3 detects a fainter source at 0.85 arcsec from the target with the same parallax ($\pi = 28.4$ mas). This separation gives a minimum mass of 0.092 $M_\odot$, supporting the idea that this closer body is much more likely to be the source of the trend.

Among the 12 stars, there are four for which AO images are available for at least two different dates. It is therefore possible to check whether the observed companion is a background star lacking significant proper or parallactic motion. Following Gonzales et al. (2020), we calculated the difference in position (offset) between the primary and the putative companion ($\Delta E, \Delta N$) at two different epochs. E and N refer to east and north coordinates, respectively. If we consider a fixed background star, it would appear to shift relatively to the target by the amount ($- \Delta E_s, \Delta N_s$), where $\Delta E_s = \Delta E_{\rm PM} + \Delta E_\pi$ and $\Delta N_s = \Delta N_{PM} + \Delta N_\pi$; $\Delta E_{\rm PM}/\Delta N_{\rm PM}$ is the proper motion variation (to the east or north) between two different dates, and $\Delta E_\pi/\Delta N_\pi$ is the variation of the parallactic motion of the primary star. We show the space motion in Fig. 17 where that of a background object is represented by the track plotted in black. The location of the companion is inconsistent with this track when it is comoving with the primary star.

6.1.1 HIP1444

The companion was observed with both NACO and NIRC2 instruments (see Fig. 15 in the latter case). In addition, *Gaia* EDR3 reports a source at nearly the same angular separation. Moreover, the proper and parallactic motions indicate that this object is bound to the target. B17 suggested that the primary could be a host to a candidate planet with an orbital period of 5082 ± 99 d, which is much smaller than the value we found. Their adopted model consists of Keplerian signals and a linear acceleration.

6.1.2 HIP62039

Our measured acceleration of combined RVs is close to the 7.19 ± 0.16 m s^{-1} yr^{-1} value estimated by B17, who did not find a periodic signal. The lack of periodicity indicates the presence of a companion with a long period.

6.1.3 HIP71803

B17 found an acceleration of -10.772 ± 0.281 m s^{-1} yr^{-1} without a periodic signal. With nearly the same acceleration, -10.592 m s^{-1} yr^{-1}, Hinkel et al. (2019) estimated a companion minimum mass of 6.8 $M_{\rm Jup}$.

6.1.4 HIP85158

Even though the orbit is not fully covered, B17 considered it as a candidate to harbour a companion with a period of 5220 ± 197 d,

Table 6. Data for HARPS targets showing a significant RV trend ($\frac{A}{T} > 10\,\mathrm{m\,s^{-1}\,yr^{-1}}$): RV amplitude, acceleration value, order of polynomial fit, cross-correlation coefficients, ρ, and significance levels, p, for the RV versus BIS and RV versus S-index variations, and chromospheric activity indicators. Stars with an asterisk have a Keplerian solution in addition to the trend, while double asterisks denote stars with confirmed companions. '–' in the $\log R'_{HK}$ column indicate stars that are not present in Boro Saikia's catalogue.

HIP/TYC	A (m s^{-1})	$\frac{A}{T}$(m s^{-1} yr^{-1})	Degree	ρ_{BIS}	pValue$_{BIS}$	ρ_S	pValue$_S$	$\log R'_{HK}$	RV jitter (m s^{-1})
948	186.4	11.7	1	0.110	0.594	−0.315	0.117	−5.171	7.411
1444∗	229.2	16.5	2	−0.017	0.812	−0.373	0.000	−4.881	9.185
5806∗∗	160.7	13.2	2	−0.221	0.010	−0.120	0.169	−4.724	14.810
10278∗∗	223.3	38.2	1	0.353	0.066	0.603	0.001	–	–
12350∗	347.1	21.3	2	0.095	0.531	0.008	0.960	−4.937	8.551
14596	434.1	27.4	2	−0.074	0.524	0.167	0.156	−4.819	9.938
19007	160.0	17.0	2	0.248	0.254	0.163	0.457	−5.200	6.134
35305	90.0	23.0	1	−0.124	0.465	−0.115	0.506	–	–
37233	662.8	41.3	3	0.056	0.671	0.363	0.005	–	–
43449	35.6	17.0	1	−0.145	0.622	0.400	0.156	–	–
45749	24.7	17.2	1	0.617	0.004	0.682	0.001	−4.710	8.506
54102∗	306.6	23.6	3	−0.280	0.088	−0.482	0.002	–	–
60689∗∗	7.5	49.1	1	0.158	0.225	0.540	0.004	–	–
61743	150.3	10.0	3	−0.041	0.824	−0.011	0.955	–	–
70610	208.0	14.8	1	0.180	0.576	0.489	0.127	−5.023	7.745
71001∗	3646.1	246.2	3	−0.167	0.386	0.230	0.239	–	–
71803	161.6	12.2	1	0.338	0.044	0.371	0.031	−4.954	8.377
76713	168.6	15.4	1	−0.065	0.762	0.083	0.707	–	–
78395	301.1	20.0	2	−0.446	0.015	0.222	0.257	–	–
81533	238.6	39.7	1	−0.742	0.000	−0.743	0.000	–	–
85158	225.2	28.8	3	0.156	0.409	0.013	0.948	−4.831	12.320
89354∗∗	132.3	18.0	3	0.190	0.165	0.214	0.117	–	–
95849∗	26.1	25.7	2	−0.818	0.000	0.828	0.000	−4.456	15.736
99385	925.1	69.5	2	−0.176	0.345	0.303	0.141	−4.401	9.333
108095∗	937.3	74.7	2	−0.155	0.380	0.489	0.003	–	–
109787	237.7	15.0	2	0.002	0.992	0.174	0.284	–	–
110156	500.4	31.5	2	−0.257	0.215	−0.103	0.640	−4.858	8.139
110843	29.8	11.7	1	0.667	0.000	0.228	0.283	−4.935	8.573
112229	70.4	15.1	1	0.526	0.001	0.197	0.241	–	–
115951∗	104.7	10.6	1	−0.144	0.238	0.333	0.005	−4.932	8.606
116374	902.2	69.1	3	0.784	0.000	−0.095	0.682	−4.761	8.377
6792-01746-1	262.2	25.6	1	0.396	0.014	−0.407	0.010	–	–
8681-00611-1	502.1	31.6	1	−0.165	0.344	0.107	0.541	–	–

an RV semi-amplitude of 29.20 ± 2.24 m s^{-1}, and an acceleration of -16.372 ± 0.432 m s^{-1} yr^{-1}. The acceleration we estimated from combining RVs is much smaller.

7 ACTIVITY INDICATORS

The variation observed in the RV curves can be related to chromospheric phenomena instead of being due to real dynamic changes in the star's centre of mass. We investigate this possibility below.

7.1 RV jitter from chromospheric activity

For the stars with putative companions (short periods or trends), we retrieved the well-known magnetic activity indicator inferred from Ca II H + K, $\log R'_{HK}$, from the catalogue of Boro Saikia et al. (2018). We then estimated the expected jitter from the calibration of Santos et al. (2000) relevant to F-, G-, and K-type stars, where $R_5 = 10^5 R'_{HK}$:

$$\begin{cases} \sigma_F(\mathrm{m\,s^{-1}}) = 9.2 \times R_5^{0.75} \\ \sigma_G(\mathrm{m\,s^{-1}}) = 7.9 \times R_5^{0.55} \\ \sigma_K(\mathrm{m\,s^{-1}}) = 7.8 \times R_5^{0.13} \end{cases} \quad (5)$$

The $\log R'_{HK}$ and RV jitter values can be found in Table 6 (HARPS) and Table 7 (SOPHIE + ELODIE) for stars with a trend (the existence

of an additional Keplerian signal and a known period are noted by a single and double asterisk, respectively).

An RV variability caused by a companion rather than by stellar activity is more likely for the stars in Table 6 that have a trend amplitude larger than five times their estimated RV jitter. Conversely, HIP45749, HIP95849, HIP98828, and HIP110843 have an RV amplitude below that limit and could have their RV variation arising from stellar activity.

7.2 Line-profile indicators

Another way to relate the RV variation to chromospheric activity is to examine the correlation between the former and some activity (line-profile) indicators, as done below.

7.2.1 Bisector velocity span

To this aim, we first use the bisector velocity span (BIS), which is the difference between the velocity of the bisector at the top and bottom of the CCF. Defined by Figueira et al. (2013) and Queloz et al. (2001), as the average of the mid-points between 60 and 90 per cent for the top and 10 and 40 per cent for the bottom. The BIS are extracted from the instrument pipeline.

Table 7. Same as Table 6, but for stars observed with SOPHIE and ELODIE.

HIP/TYC	A (m s^{-1})	$\frac{A}{T}$ (m s^{-1} yr^{-1})	Degree	ρ_{BIS}	pValue$_{BIS}$	ρ_S	pValue$_S$	$\log R'_{HK}$	RV jitter (m s^{-1})
SOPHIE									
23209*	130.3	13.0	1	–	–	-0.241	0.217	–	–
26037	1250.3	90.0	2	-0.134	0.622	-0.602	0.006	-4.909	8.864
29611	402.3	45.3	1	-0.206	0.227	-0.073	0.683	–	–
31849	275.7	46.6	1	-0.895	0.000	0.459	0.014	–	–
32906	167.3	41.2	2	0.261	0.367	-0.699	0.003	–	–
35198	59.8	63.7	2	-0.052	0.842	-0.184	0.494	–	–
44324	216.7	22.2	1	–	–	0.133	0.587	–	–
61157	223.4	27.6	1	0.114	0.605	-0.047	0.832	–	–
63346	192.4	22.4	2	-0.270	0.058	-0.282	0.047	–	–
68134	385.8	31.5	1	–	–	0.305	0.219	–	–
71291	779.7	66.8	1	0.527	0.064	-0.398	0.060	–	–
74702	68.4	39.3	3	-0.846	0.000	0.567	0.011	-4.457	9.177
76751	916.5	81.2	2	-0.195	0.544	0.040	0.908	–	–
77718*	110.4	22.1	1	0.043	0.765	-0.024	0.881	–	–
85653	130.2	11.6	1	0.406	0.026	0.206	0.242	-4.928	8.654
91658	31.6	31.8	1	-0.312	0.106	-0.029	0.884	–	–
96184*	120.3	11.6	1	–	–	-0.343	0.017	–	–
98828	37.0	10.1	2	-0.097	0.720	0.827	0.003	-4.707	8.515
104587*	110.2	12.0	1	0.843	0.000	0.310	0.004	-4.994	7.814
111977	91.0	10.1	3	–	–	-0.033	0.899	–	–
113086	222.6	19.9	1	0.261	0.367	0.239	0.325	-4.815	12.665
114210	77.3	12.6	2	0.190	0.481	0.125	0.589	-4.735	14.5387
115714**	321.5	39.7	1	0.197	0.152	-0.213	0.033	–	–
1991-01087-1*	27.8	25.7	1	-0.228	0.075	-0.313	0.059	–	–
ELODIE									
19422	156.2	17.1	1	–	–	–	–	–	–
24205**	202.0	34.0	3	–	–	–	–	–	–
61157	191.8	79.5	1	–	–	–	–	–	–
77718	120.3	14.8	1	–	–	–	–	–	–
80264	96.3	14.0	3	–	–	–	–	–	–
80902**	110.6	12.4	2	–	–	–	–	–	–
85653	144.6	16.1	1	–	–	–	–	–	–
108602	128.5	17.6	1	–	–	–	–	–	–

Table 8. Trend stars with model standard deviation exceeding 100 m s^{-1} in 10 yr, 12 yr, and during the time span. Asterisk symbols have the same meaning as in Table 6.

HIP/TYC	T (yr)	σ_{10} (m s^{-1})	σ_{12} (m s^{-1})	σ_T (m s^{-1})
HARPS				
5806**	12.2	–	113.5	116.4
37233	16.1	194.4	308.5	637.4
64295**	6.3	–	–	103.2
71001*	14.8	1175.0	2358.4	4950.0
99385	13.3	221.1	270.8	304.2
108095*	12.6	144.8	156.1	158.3
116374	13.0	191.3	192.6	187.6
8681-00611-1	15.9	–	109.4	144.9
SOPHIE				
26037	13.9	809.4	1056.5	1316.7
29611	8.9	–	–	116.1
32906	4.1	–	–	214.8
68134	12.3	–	109.1	111.4
71291	11.7	192.9	231.5	225.1
74702	1.7	–	–	196.9
76751	11.3	346.8	434.1	402.1
114210	6.1	–	–	106.8
ELODIE				
80264	6.9	–	–	108.1
80902**	8.9	–	–	102.7

If the BIS and RV data are independent, the variability signal may have its origin in an unseen companion. However, a negative correlation indicates that the RV variations arise from stellar activity, as concluded by Queloz et al. (2001) and Martínez Fiorenzano et al. (2005) for HD 166435. On the other hand, a positive correlation may be the signature of a blended system or a substellar companion, as in HD 41004 where Santos et al. (2002) attributed the variation to a brown dwarf companion to the secondary. In the same vein, Martínez Fiorenzano et al. (2005) showed that the positive correlation between RVs and bisector spans in HD 8071 is due to contamination by a companion with a non-linear dependence. However, Lovis et al. (2011) noted that a positive correlation could also indicate that a magnetic cycle is the source of the RV variation. Zechmeister et al. (2013) pointed out that the physical correlation cannot be confirmed on firm statistical grounds unless both variables vary with an identical period. In this case, the (sub)stellar companion option becomes invalid.

We computed Pearson's correlation coefficients (hereafter ρ) between the RV and BIS data, along with the associated confidence level, p. The ρ and p values are summarized in the fifth and sixth columns of Table 6 (HARPS) and Table 7 (SOPHIE + ELODIE) for stars with trends.

Among the stars with a trend having an acceleration greater than or equal to 10 m s^{-1} yr^{-1}, four have their RVs significantly anticorrelated to BIS, which indicates that the RV variation can

Table 9. Data for stars in common between HARPS, SOPHIE, ELODIE, and B17 showing a significant RV trend ($\frac{A}{T} > 10 \, \mathrm{m \, s^{-1} \, yr^{-1}}$): RV amplitude, acceleration value, order of polynomial fit, shift between HARPS and B17, HARPS and SOPHIE, HARPS and ELODIE, and ELODIE and SOPHIE. Asterisk symbols have the same meaning as in Table 6.

HIP/TYC	A (m s^{-1})	$\frac{A}{T}$ (m s^{-1} yr^{-1})	Degree	shift$_{\mathrm{HB17}}$ (m s^{-1})	shift$_{\mathrm{HS}}$ (m s^{-1})	shift$_{\mathrm{HE}}$ (m s^{-1})	shift$_{\mathrm{ES}}$ (m s^{-1})
1444	427.9	20.4	2	28822.8 ± 0.7	–	–	–
5806**	154.1	12.6	2	–	−25.1 ± 8.0	–	–
7404	164.5	12.8	3	–	−108.8 ± 7.7	–	–
14614	246.9	11.4	3	–	18.2 ± 2.2	−95 ± 15	–
26037	1250.5	75.5	2	–	–	–	−326 ± 16
29611	669.8	45.3	1	–	–	–	2.3 ± 16.1
42575	474.3	150.0	1	–	–	–	288 ± 29
61157	578.8	43.0	3	–	–	–	−112 ± 15
63346	267.2	19.2	3	–	–	–	−5.4 ± 11.7
68134	486.6	31.5	1	–	–	–	71 ± 23
71803	223.1	11.4	2	12953 ± 1	–	–	–
85158	295.2	18.5	3	−24065 ± 0.8	–	–	–
99385	925.2	69.5	2	22239 ± 2	–	–	–
104587	164.4	13.4	1	–	–	–	75 ± 11
108602	307.5	17.8	1	–	–	–	277 ± 23
113086	209.5	12.2	2	–	–	–	31 ± 11
115714**	448.4	28.4	1	–	–	–	140 ± 10

Table 10. Similar to Table 8, but for combined data sets. Stars in bold only exceed the *Gaia* threshold when data from different instruments are combined. Asterisk symbols have the same meaning as in Table 6.

HIP	T (yr)	σ_{10} (m s^{-1})	σ_{12} (m s^{-1})	σ_T (m s^{-1})
5806**	12.2	–	113.9	116.8
7404	12.9	–	160.2	194.9
26037	16.6	771.8	1011.4	1665.6
29611	14.8	130.8	157.0	193.4
42575	3.16	–	–	136.9
61157	13.5	–	138.3	181.1
68134	15.4	–	109.0	139.9
85158	15.9	103.0	142.3	245.0
99385	13.3	219.8	269.2	302.4

Figure 15. HIP 1444 NIRC2 AO image obtained on 09-08-2013 made available in the Keck Observatory Archive by the programme PI: Barclay. We cropped the image and inverted the colours. The distance between the objects is 47.15 ± 0.33 au and their flux ratio is 14.58 in the *K* band. *Gaia* source positions at epoch 2016.0 (orange squares) were overplotted using Aladin Sky Atlas. The arrow shows the primary motion with the modulus corresponding to the proper motion.

be related to chromospheric phenomena. It concerns HIP5806, HIP78395, HIP81533, and HIP95849.

However, as mentioned above, a significant correlation does not provide a firm identification of the source of the variation, and doubt remains for HIP81533 where a companion is clearly detected through AO SPHERE imaging (Section 6.1), but we are unsure whether it is causing the trend. However, as the trend's acceleration is high, we doubt it would be caused by activity.

There are six trend stars with RVs positively correlated to BIS and without any companion detected previously (RV or imaging). For those, the variation can be caused by a blended system or a magnetic activity cycle. Among these stars, two have a high acceleration, which is more likely induced by a companion: HIP116374 and TYC6792-01746-1.

As for SOPHIE targets, a significant, positive correlation is present for HIP85653 and HIP104587, which could indicate the cause of the trend to be a magnetic cycle. HIP31849 and HIP74702 have a significant correlation between RV and BIS; however, they have high acceleration.

7.2.2 The S-index

The S-index is dependent on the strength of the magnetic field and compares the relative flux of the Fraunhofer emission lines (H&K) of Ca II to the continuum value. It is used to determine stellar activity cycles and rotation periods.

We computed this index using the method described by Lovis et al. (2011) where *H* and *K* are the total fluxes in the bands centred at 3933.664 Å (*K*) and 3968.470 Å (*H*), *R* and *V* are the values measured in adjacent continuum passbands, and α is a calibration constant:

$$S = \alpha \frac{H + K}{R + V} \ . \tag{6}$$

As the activity level increases, active regions in which convection is frozen cover a larger fraction of the stellar surface. It implies that convective blueshift is globally reduced and the lines are slightly shifted to the red. As a net result, a positive correlation between RVs and S-index is expected.

Table 11. Astrometric and photometric results for the stars observed with AO instruments allowing us to compare *Gaia* and AO angular separations (θ_{Gaia} and θ_{AO}), as well as minimum dynamical and photometric masses (M_{min} and M_{phot}).

HIP	$\gamma_r (\text{m s}^{-1}\,\text{yr}^{-1})$	θ_{Gaia} (arcsec)	θ_{AO} (arcsec)	a (au)	K or J (mag)	M_{min} ($M_\odot$)	M_{phot} ($M_\odot$)	P (yr)	Instrument
1444	18.574 ± 0.052	1.794	1.574 ± 0.020	42.3 ± 0.6	5.744 (K)	0.48 ± 0.01	0.483	223.6 ± 7.2	NACO
7396	21.177 ± 0.198	–	0.246 ± 0.025	9.4 ± 1.0	6.054 (H)	0.03 ± 0.01	0.471	26.0 ± 4.2	NACO
52720	− 5.154 ± 0.211	1.677	1.691 ± 0.023	94.2 ± 1.4	6.093 (K)	0.67 ± 0.04	0.432	821 ± 53	NACO
58558	2.834 ± 0.313	–	1.617 ± 0.019	67.9 ± 0.7	8.793 (J)	0.19 ± 0.03	0.218	520 ± 17	NACO
62039	7.118 ± 0.052	1.293	1.309 ± 0.014	58.8 ± 0.7	7.667 (J)	0.36 ± 0.01	0.329	395 ± 7	NIRC2
71803	− 10.941 ± 0.098	–	0.547 ± 0.020	29.6 ± 1.1	9.404 (J)	0.14 ± 0.01	0.176	143 ± 11	NIRC2
81533	39.727 ± 0.374	–	0.359 ± 0.025	25.3 ± 1.8	6.376 (H)	0.37 ± 0.04	0.426	107 ± 9	SPHERE
85158	− 11.344 ± 0.274	–	0.680 ± 0.019	22.5 ± 0.7	6.809 (K)	0.08 ± 0.01	0.332	90 ± 4	NIRC2
99385	− 64.247 ± 0.519	–	0.876 ± 0.048	13.9 ± 0.6	8.119 (K)	0.18 ± 0.02	0.202	54 ± 4	NACO
102580	9.2013 ± 0.908	2.401	2.109 ± 0.026	78.0 ± 1.1	8.123 (K)	0.82 ± 0.10	0.202	645 ± 20	NACO
105606	7.263 ± 0.838	0.849	3.318 ± 0.019	116.4 ± 0.8	10.010 (K)	1.43 ± 0.18	0.112	1224 ± 26	NACO
110843	− 11.709 ± 1.283	–	1.089 ± 0.025	40.2 ± 1.0	6.554 (K)	0.28 ± 0.04	0.361	216 ± 10	NACO
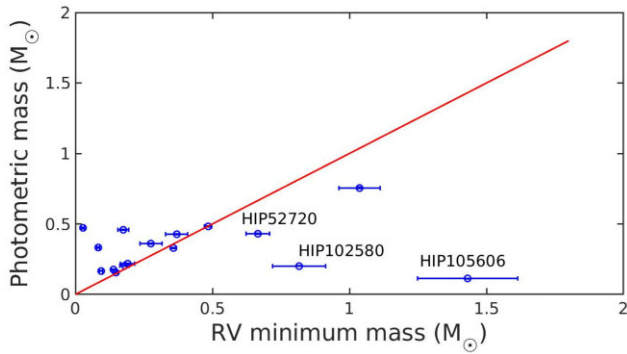
Figure 16. Comparison between photometric masses from AO and the minimum dynamic masses deduced from the trend acceleration. The 1:1 relation is represented by the red line. Stars above that line have companions that are likely responsible for the RV acceleration. Stars below it (HIP52720, HIP102580, and HIP105606) have visual companions not responsible for the RV acceleration at the corresponding measured separation.

The ρ and p-values diagnosing a possible correlation between these two quantities are listed in columns 7 and 8 of Table 6 (HARPS) and Table 7 (SOPHIE + ELODIE) for the stars with a trend.

There are eight trend stars with RV positively correlated to the S-index for which we assume that the long-term RV variation may be attributed to a magnetic cycle. HIP45749 and HIP71803 have a positive correlation with BIS confirming that their RV variation is indeed caused by a magnetic cycle.

The RV variations exhibited by HIP1444 are confirmed to be related to a companion by AO imaging, although it shows a significant correlation with the S-index. Even though we are not sure if the companion in AO imaging causes the trend in the case of HIP81533, it is very unlikely to be activity related.

The SOPHIE stars with a positive correlation between RVs and S-index and low acceleration value are HIP98828 and HIP104587 (for which the BIS is also positively correlated to RVs). Those with high acceleration value are HIP31849 and HIP74702.

8 CONCLUSION

We present a work aiming at confirming the status of a sample of 2351 stars as RV standards for the *Gaia* mission. We estimated the offset of our RVs relative to other instruments and placed the zero-point by adopting HARPS measurements as the reference. We find a

mean absolute difference of 240.4 m s^{-1} between our measurements and those determined by the instrument pipelines.

We looked for RV variability due to the presence of a companion or due to the existence of stellar activity/magnetism. Furthermore, we find stars having a linear or polynomial trend variation for which the period cannot be determined with the actual data because it is longer than the observational baseline. AO help in a few cases confirming the presence of distant companions potentially inducing a long-term trend, although the physical association must be proven. Five stars with AO data have a visual companion lying at an angular separation consistent with the observed RV amplitude, but it is not the case for the three others. Among the first category, the analysis of the proper motions supports the bound status of the secondaries in HIP1444, HIP62039, HIP71803, and HIP99385. As the stars exhibiting an RV trend have incomplete orbital coverage, they should be monitored on a long-term basis. The trends with high acceleration, on the other hand, could indicate that the companion orbiting these stars is a brown/red dwarf. However, as the RV variation can also be caused by chromospheric activity, we checked for possible correlations between the RV and activity data to ascertain that the observed RV variations have their origin in a low-mass companion.

Stars with an RV model scatter (orbital and/or trend) exceeding the threshold required for the *Gaia* mission, 300 m s^{-1}, should be excluded from the calibrations for *Gaia* DR4. From the HARPS sample, it concerns five stars with a trend only (HIP37233, HIP64295, HIP99385, HIP116374, and TYC8681-00611-1), three stars with a Keplerian solution only (HIP26394, HIP62534, and HIP113834), and three stars with both trend and Keplerian solution (HIP5806, HIP71001, and HIP108095). Additional variable stars are identified through their SOPHIE observations: HIP26037, HIP29611, HIP32906, HIP68134, HIP71291, HIP74702, HIP76751, HIP114210, HIP115714, and TYC3239-00992-1. The only ELODIE stars that show RV variability are HIP80264 and HIP80902. After combining data from several instruments, four more stars can be considered variable: HIP7404, HIP42575, HIP61157, and HIP85158. All the calibration stars not fulfilling the *Gaia* criterion for a constant RV are listed in Table 12. Other less obvious candidates are discussed in Section 6. Stars for which the weighted standard deviation applied on data, σ_{RV}, exceeds the variability threshold set by CS13 are shown in Fig. 18. Because this subset constitutes a tiny fraction of our sample, it supports the validity of the CS18 catalogue as a pool of RV calibrators for the RVS onboard *Gaia*.
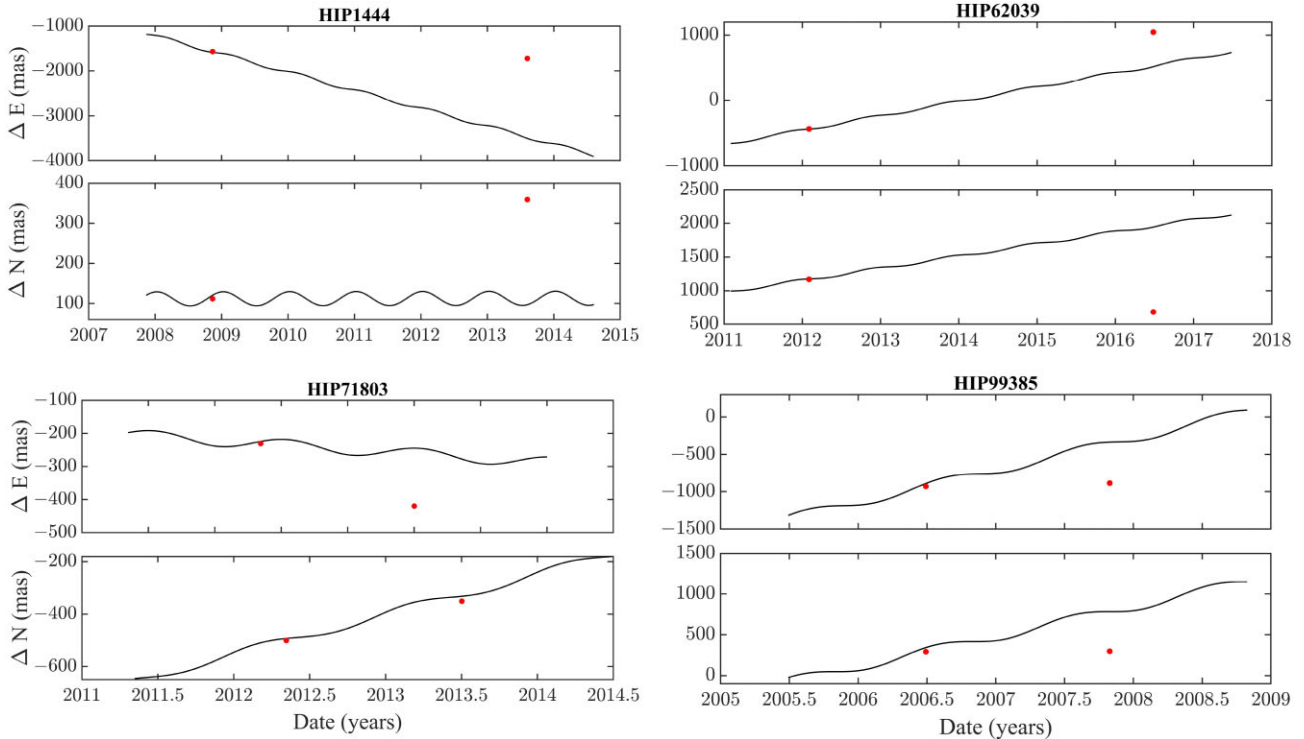
Figure 17. Astrometric data for the four stars observed in AO at different epochs. The black curves show the motion of a background object. The red points are the astrometric measurements of the visual companion. As the companion does not follow the motion of a background object, it is likely bound to the primary.

Table 12. Targets with RV scatter greater than the *Gaia* threshold, which should be removed from *Gaia* DR4.

HIP/TYC	Instrument
7404	H-S
5806	H
26037	S
26394	H
29611	S
32906	S
37233	H
42575	S-E
61157	S-E
62534	H
64295	H
68134	S
71001	H
71291	S
74702	S
76751	S
80264	E
80902	E
85158	H-B17
99385	H
108095	H
113834	H
114210	S
115714	S
116374	H
3239-00992-1	S
8681-00611-1	H
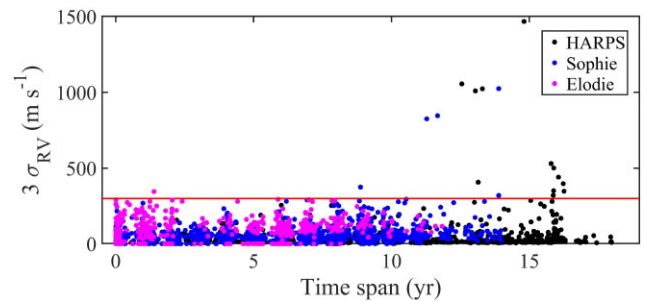
Figure 18. RV variation as a function of the time span with the *Gaia* RV variability threshold ($300 \, \mathrm{m \, s^{-1}}$) depicted by the red horizontal line.

This study is based on data obtained from the European Southern Observatory (ESO) Science Archive Facility with DOI(s): https://doi.org/10.18727/archive/33 and on data retrieved from the SOPHIE archive at Observatoire de Haute-Provence (OHP), available at atlas.obs-hp.fr/sophie.

DATA AVAILABILITY

The data underlying this paper are available in the paper and in its online supplementary material.

This paper made use of data publicly available at the CDS via https://cdsarc.cds.unistra.fr/viz-bin/cat/I/345 (CS18), https://cdsarc.cds.unistra.fr/viz-bin/cat/J/A+A/636/A74 (T20), https://cdsarc.cds.unistra.fr/viz-bin/cat/J/AJ/153/208 (B17).

REFERENCES

Anderson T. W., Darling D. A., 1952, Ann. Math. Stat., 23, 193
Andrae R., Schulze-Hartung T., Melchior P., 2010, preprint (arXiv:1012.3754)
Anglada-Escudé G., Butler R. P., 2012, ApJS, 200, 15
Bailer-Jones C., Rybizki J., Fouesneau M., Demleitner M., Andrae R., 2021, AJ, 161, 147
Bean J. L., McArthur B. E., Benedict G. F., Harrison T. E., Bizyaev D., Nelan E., Smith V. V., 2007, AJ, 134, 749
Beuzit J.-L. et al., 2010, In the Spirit of Lyot 2010. p. E44
Boro Saikia S. et al., 2018, A&A, 616, A108
Butler R. P. et al., 2017, AJ, 153, 208 (B17)
Cropper M. et al., 2018, A&A, 616, A5
David M., Blomme R., Frémat Y., Damerdji Y., Delle Luche C., Gosset E., Katz D., Viala Y., 2014, A&A, 562, A97
De Laverny P., Recio-Blanco A., Worley C. C., Plez B., 2012, A&A, 544, A126
Donati J. -F., 1997, MNRAS, 291, 658
Dumusque X. et al., 2012, Nature, 491, 207
Figueira P., Santos N. C., Pepe F., Lovis C., Nardetto N., 2013, A&A, 557, A93
Frémat Y. et al., 2017, A&A, 597, A10
Gaia Collaboration et al., 2016, A&A, 595, A1
Gaia Collaboration et al., 2018, A&A, 616, A1
Gaia Collaboration et al., 2021, A&A, 649, A1
Glebocki R., Gnacinski P., 2005, in Favata F., Hussain G.~A.~J, Battrick B, rds, 13th Cambridge Workshop on Cool Stars, Stellar Systems and the Sun. Vol. 560, p. 571
Gonzales E. J., Crepp J. R., Bechter E. B., Wood C. M., Johnson J. A., Montet B. T., Isaacson H., Howard A. W., 2020, ApJ, 893, 27
Gosset E., Royer P., Rauw G., Manfroid J., Vreux J. M., 2001, MNRAS, 327, 435
Gray D. F., 2021, The Observation and Analysis of Stellar Photospheres. Cambridge Univ. Press, Cambridge
Gustafsson B. et al., 2008, A&A, 486, 951
Hébrard G. et al., 2016, A&A, 588, A145
Heck A., Manfroid J., Mersch G., 1985, A&AS, 59, 63
Hinkel N. R., Unterborn C., Kane S. R., Somers G., Galvez R., 2019, ApJ, 880, 49
Husser T.-O., Wende-von Berg S., Dreizler S., Homeier D., Reiners A., Barman T., Hauschildt P. H., 2013, A&A, 553, A6
Krystek M., Anton M., 2007, Meas. Sci. Technol., 18, 3438
Lenzen R. et al., 2003, in Masanori I, F~M Moorwood A, eds, Instrument Design and Performance for Optical/Infrared Ground-based Telescopes. Vol, 4841, SPIE, p. 944
Liu M. C., Fischer D. A., Graham J. R., Lloyd J. P., Marcy G. W., Butler R. P., 2002, ApJ, 571, 519
Lo Curto G. et al., 2015, The Messenger, 162, 9
Lovis C. et al., 2011, preprint (arXiv:1107.5325)

Martínez Fiorenzano A. F., Gratton R. G., Desidera S., Cosentino R., Endl M., 2005, A&A, 442, 775
MATLAB, 2022, version 9.12.0 (R2022a). The MathWorks Inc., Natick, MA
Merle T. et al., 2020, A&A, 635, A155
Moultaka J., Ilovaisky S., Prugniel P., Soubiran C., 2004, PASP, 116, 693
Moutou C. et al., 2011, A&A, 527, A63
Nordström B., Stefanik R. P., Latham D. W., Andersen J., 1997, A&AS, 126, 21
Noyes R. W. et al., 2008, ApJ, 673, L79
Palacios A., Gebran M., Josselin E., Martins F., Plez B., Belmas M., Lebre A., 2010, A&A, 516, A13
Pecaut M. J., Mamajek E. E., 2013, ApJS, 208, 9
Petit P. et al., 2014, PASP, 126, 469
Pourbaix D. et al., 2004, A&A, 424, 727
Press W. H., Teukolsky S. A., Vetterling W. T., Flannery B. P., 1986, Numerical Recipes in Fortran 77, Cambridge university press, New York
Queloz D. et al., 2001, A&A, 379, 279
Raghavan D. et al., 2010, ApJS, 190, 1
Rickman E., Ségransan D., Hagelberg J., Beuzit J.-L., Cheetham A., Delisle J.-B., Forveille T., Udry S., 2020, A&A, 635, A203
Robertson P., Endl M., Cochran W. D., Dodson-Robinson S. E., 2013, ApJ, 764, 3
Rousset G. et al., 2003, in Wizinowich P. L., Bonaccini D., eds, Proc. SPIE Conf. Ser.Vol. 4839, Adaptive Optical System Technologies II. SPIE, Bellingham, p. 140
Santos N. C. et al., 2002, A&A, 392, 215
Santos N. C. et al., 2014, A&A, 566, A35
Santos N. C., Mayor M., Naef D., Pepe F., Queloz D., Udry S., Blecha A., 2000, A&A, 361, 265
Sartoretti P. et al., 2018, A&A, 616, A6
Soubiran C. et al., 2018, A&A, 616, A7 (CS18)
Soubiran C., Jasniewicz G., Chemin L., Crifo F., Udry S., Hestroffer D., Katz D., 2013, A&A, 552, A64(CS13)
Soubiran C., Le Campion J.-F., Brouillet N., Chemin L., 2016, A&A, 591, A118
Stassun K. G., Collins K. A., Gaudi B. S., 2017, AJ, 153, 136
Torres G., 1999, PASP, 111, 169
Trifonov T., Tal-Or L., Zechmeister M., Kaminski A., Zucker S., Mazeh T., 2020, A&A, 636, A74 (T20)
Venner A., Vanderburg A., Pearce L. A., 2021, AJ, 162, 12
Wittenmyer R. A., Clark J. T., Zhao J., Horner J., Wang S., Johns D., 2019, PASP, 484, 5859
Zechmeister M. et al., 2013, A&A, 552, A78
Zechmeister M., Kürster M., 2009, A&A, 496, 577

SUPPORTING INFORMATION

Supplementary data are available at *MNRAS* online.

Table S1. List of targets: target ID, coordinates (α, δ) at the specific epoch, visual apparent magnitude, V, spectral type taken from CS18, SpT, total time span, T, minimum and maximum S/N values, total number of analysed spectra, N_{init}, the final number of measurements after filtering, N, the number of additional spectra compared to CS18, N_{add}, and the instrument used.

Table S2. Stellar parameters of the best-fitting synthetic spectra (T_{eff}, $\log g$, [Fe/H], and [α/Fe]), along with vbroad, our mean measured RV, $\langle RV_m \rangle$, and the median RV from CS18, $\langle RV_{\text{CS18}} \rangle$.

Table S3. Orthogonal regression coefficients of the fit between our measured and T20 RVs.

Please note: Oxford University Press is not responsible for the content or functionality of any supporting materials supplied by the authors. Any queries (other than missing material) should be directed to the corresponding author for the article.
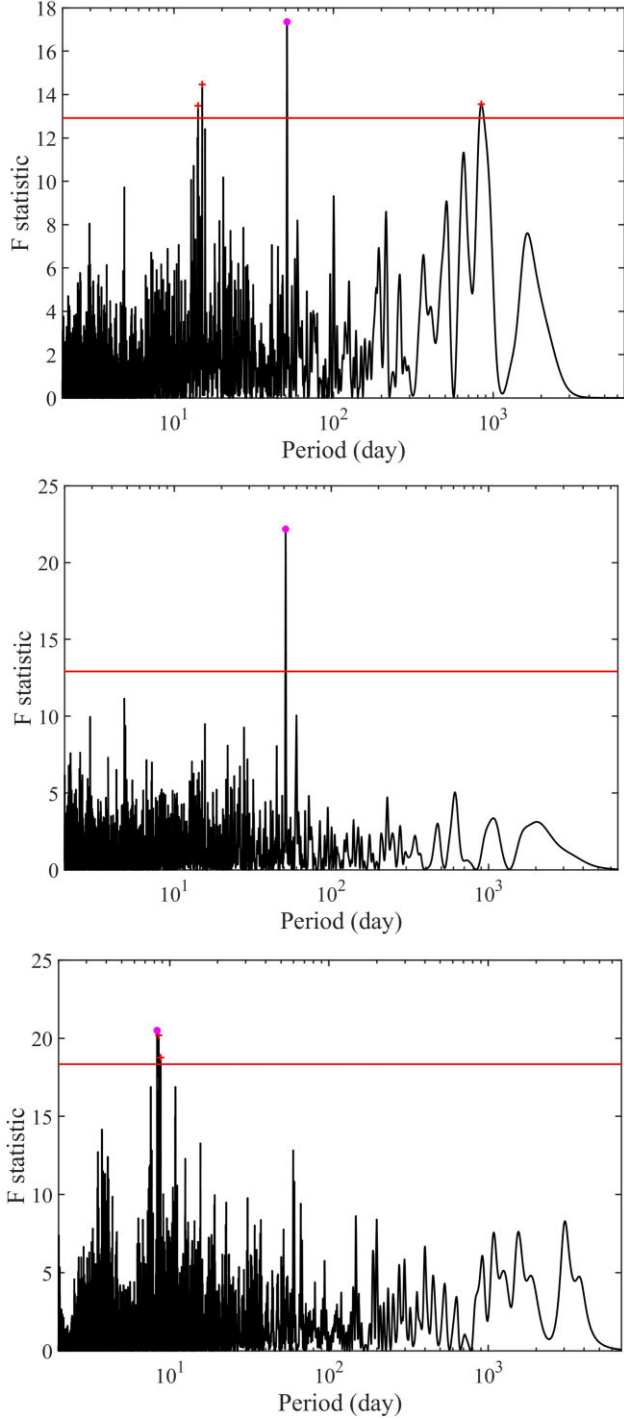
APPENDIX A: ORBITAL SOLUTIONS

Figure A1. Top panel: periodogram of HIP5806 with the orbital period of 806 d. This period does not correspond to the highest peak, but it gives the best solution. Middle panel: periodogram showing HIP5806's third period, 51.154 d. Bottom panel: periodogram of HIP108095 with the highest peak period of 8.53127 d. Same symbols as in Fig. 12.
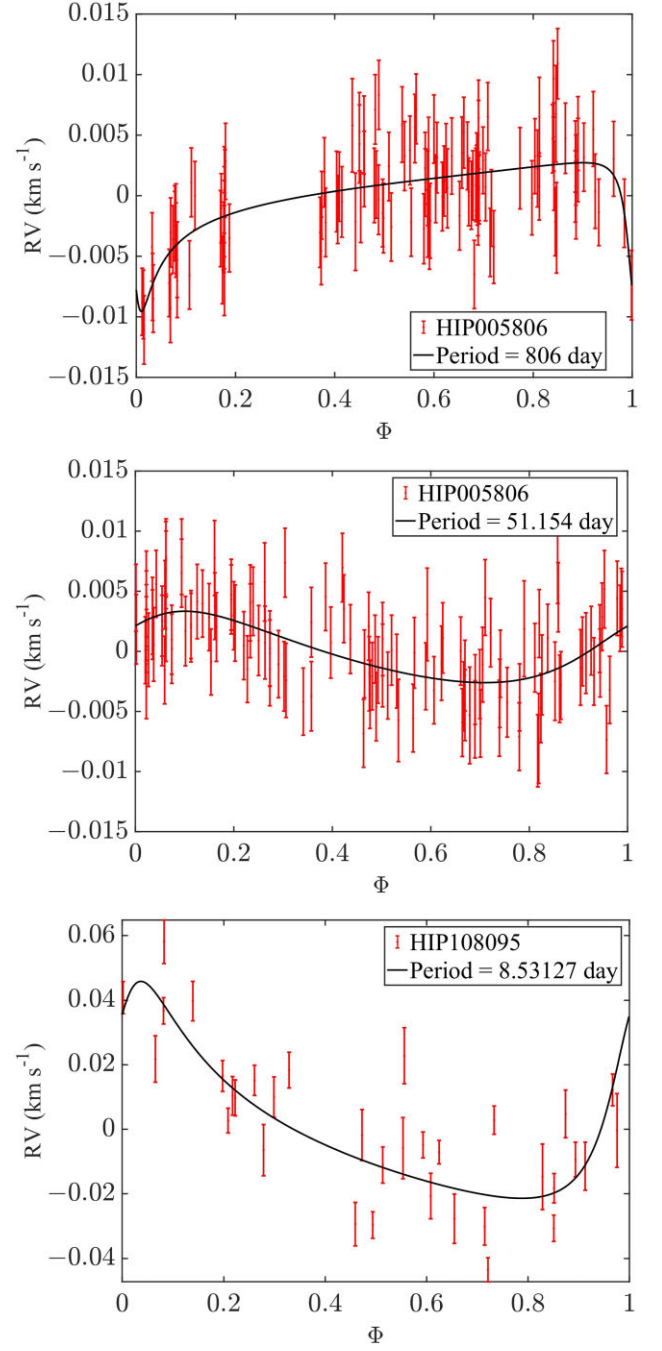

Figure A2. Phase-folded RV curve for HIP5806 with the orbital periods of 806 d (top panel), and of 51.154 d (middle panel), and for HIP108095 with the orbital period of 8.53127 d (bottom panel).

APPENDIX B: COMPUTATION OF THE STANDARD DEVIATION FOR TREND SOLUTION

$$\sigma^2(P_n(\mathrm{RV})) = \sum_{i=1}^{i=n}\left[\frac{i^2\,a_i^2\,T^{2i}}{(2i+1)(i+1)^2} + 2\sum_{j=i+1}^{j=n}\frac{i\,j\,a_i\,a_j\,T^{i+j}}{(i+j+1)(i+1)(j+1)}\right]$$

(B1)

where

$$P_n(\mathrm{RV}(t_k)) = \sum_{i=0}^{i=n} a_i\, t_k^i \qquad (B2)$$

and t_k is uniformly distributed in $[0, T]$.
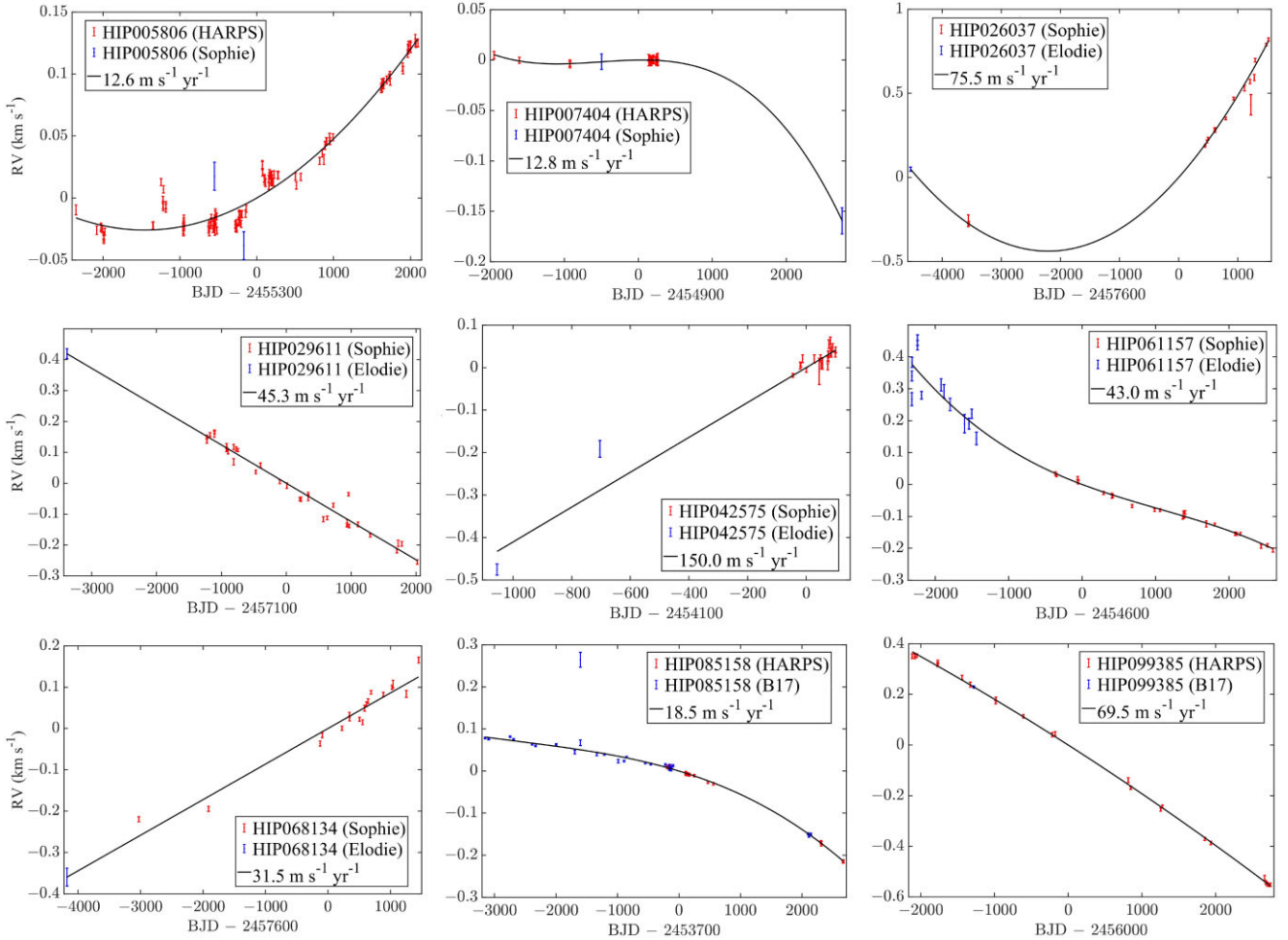
APPENDIX C: RV TRENDS

Figure C1. RV variations of trend stars with $\sigma_{\mathrm{Model}} \geq 100\ \mathrm{m\,s^{-1}}$ (the acceleration is indicated in each panel). Top row: HIP5806, HIP7404, and HIP026037. Middle row: HIP29611, HIP42575, and HIP61157. Bottom row: HIP68134, HIP85158, and HIP99385.

This paper has been typeset from a TEX/LATEX file prepared by the author.